



Disk-Jet Coupling in the 2017/2018 Outburst of the Galactic Black Hole Candidate X-Ray Binary MAXI J1535-571

Downloaded from: <https://research.chalmers.se>, 2026-06-17 04:17 UTC









Citation for the original published paper (version of record):

Russell, T., Tetarenko, A., Miller-Jones, J. et al (2019). Disk-Jet Coupling in the 2017/2018 Outburst of the Galactic Black Hole Candidate X-Ray Binary MAXI J1535-571. *Astrophysical Journal*, 883(2). <http://dx.doi.org/10.3847/1538-4357/ab3d36>

N.B. When citing this work, cite the original published paper.



Disk–Jet Coupling in the 2017/2018 Outburst of the Galactic Black Hole Candidate X-Ray Binary MAXI J1535–571

T. D. Russell¹ , A. J. Tetarenko^{2,3} , J. C. A. Miller-Jones⁴ , G. R. Sivakoff³ , A. S. Parikh¹, S. Rapisarda^{1,5}, R. Wijnands¹, S. Corbel^{6,7}, E. Tremou⁶ , D. Altamirano⁸, M. C. Baglio⁹ , C. Ceccobello¹⁰, N. Degenaar¹, J. van den Eijnden¹, R. Fender¹¹, I. Heywood^{11,12}, H. A. Krimm¹³, M. Lucchini¹, S. Markoff¹ , D. M. Russell⁹, R. Soria^{14,15} , and P. A. Woudt¹⁶

¹ Anton Pannekoek Institute for Astronomy, University of Amsterdam, Science Park 904, NL-1098 XH Amsterdam, The Netherlands; t.d.russell@uva.nl

² East Asian Observatory, 660 N. A‘ohoku Place, University Park, Hilo, Hawaii 96720, USA

³ Department of Physics, University of Alberta, CCIS 4-181, Edmonton, AB T6G 2E1, Canada

⁴ International Centre for Radio Astronomy Research—Curtin University, GPO Box U1987, Perth, WA 6845, Australia

⁵ Shanghai Astronomical Observatory and Key Laboratory for Research Galaxies and Cosmology, Chinese Academy of Sciences, 80 Nandan Road, Shanghai 200030, People’s Republic of China

⁶ AIM, CEA, CNRS, Université Paris Diderot, Sorbonne Paris Cité, Université Paris-Saclay, F-91191 Gif-sur-Yvette, France

⁷ Station de Radioastronomie de Nançay, Observatoire de Paris, PSL Research University, CNRS, Univ. Orléans, F-18330 Nançay, France

⁸ School of Physics and Astronomy, University of Southampton, Highfield SO17 1BJ, UK

⁹ New York University Abu Dhabi, P.O. Box 129188, Abu Dhabi, United Arab Emirates

¹⁰ Department of Space, Earth and Environment, Chalmers University of Technology, Onsala Space Observatory, SE-439 92 Onsala, Sweden

¹¹ Astrophysics, Department of Physics, Denys Wilkinson Building, Keble Road, Oxford OX1 3RH, UK

¹² Centre for Radio Astronomy Techniques and Technologies, Department of Physics and Electronics, Rhodes University, Grahamstown 6140, South Africa

¹³ National Science Foundation, 2415 Eisenhower Avenue, Alexandria, VA 22314, USA

¹⁴ College of Astronomy and Space Sciences, University of the Chinese Academy of Sciences, Beijing 100049, People’s Republic of China

¹⁵ Sydney Institute for Astronomy, School of Physics A28, The University of Sydney, Sydney, NSW 2006, Australia

¹⁶ Inter-University Institute for Data-Intensive Astronomy, Department of Astronomy, University of Cape Town, Private Bag X3, Rondebosch 7701, South Africa

Received 2019 May 30; revised 2019 August 7; accepted 2019 August 19; published 2019 October 4

Abstract

MAXI J1535–571 is a Galactic black hole candidate X-ray binary that was discovered going into outburst in 2017 September. In this paper, we present comprehensive radio monitoring of this system using the Australia Telescope Compact Array, as well as the MeerKAT radio observatory, showing the evolution of the radio jet during its outburst. Our radio observations show the early rise and subsequent quenching of the compact jet as the outburst brightened and then evolved toward the soft state. We constrain the compact jet quenching factor to be more than 3.5 orders of magnitude. We also detected and tracked (for 303 days) a discrete, relativistically moving jet knot that was launched from the system. From the motion of the apparently superluminal knot, we constrain the jet inclination (at the time of ejection) and speed to $\leq 45^\circ$ and $\geq 0.69c$, respectively. Extrapolating its motion back in time, our results suggest that the jet knot was ejected close in time to the transition from the hard intermediate state to soft intermediate state. The launching event also occurred contemporaneously with a short increase in X-ray count rate, a rapid drop in the strength of the X-ray variability, and a change in the type-C quasi-periodic oscillation (QPO) frequency that occurs >2.5 days before the first appearance of a possible type-B QPO.

Key words: accretion, accretion disks – black hole physics – ISM: jets and outflows – X-rays: binaries – radio continuum: stars – stars: individual (MAXI J1535–571)

1. Introduction

Accreting stellar-mass black hole (BH) X-ray binaries (XRBs) launch powerful jets that are observable from radio to infrared (IR) wavelengths (and possibly even up to the X-ray and even γ -ray band). These jets are capable of carrying away a significant fraction of the accretion power and depositing large amounts of energy into their surroundings (e.g., Gallo et al. 2005; Russell et al. 2007; Tetarenko et al. 2018) that may alter star formation, galaxy evolution, and even the distribution of matter in the universe (e.g., Silk & Rees 1998; Barkana & Loeb 2001; Mirabel et al. 2011; Fabian 2012). While jet production appears to be fundamentally linked to the process of accretion, the exact nature of the coupling remains poorly understood (e.g., Fender et al. 2004), and how jets are launched, accelerated, and collimated by the accretion inflow is not yet clear.

BH XRBs occasionally go through episodic phases of enhanced accretion (called outbursts) where they brighten significantly as the accretion flow (e.g., Belloni 2010) and the jets change dramatically (e.g., Corbel et al. 2004; Fender et al. 2004; Fender 2006; Fender & Gallo 2014). These systems evolve

through their full outburst cycles on timescales of weeks, months, and sometimes years, allowing the full evolution of their accretion and jet duty cycles to be observed in detail. This is one of the reasons that XRBs are excellent laboratories to study BH accretion and jet phenomena.

During the initial rising phase of a typical outburst, BH XRBs are in a hard X-ray spectral state (see, e.g., Belloni 2010, for a review on the accretion states). This state is characterized by a hard power-law component in the X-ray spectrum (e.g., Narayan & Yi 1995) and flat or slightly inverted radio spectrum ($\alpha \gtrsim 0$, where the radio flux, S_ν , is proportional to the frequency, ν , such that $S_\nu \propto \nu^\alpha$; e.g., Fender 2001) from a persistent, partially self-absorbed compact jet (e.g., Corbel et al. 2000; Dhawan et al. 2000; Stirling et al. 2001). This flat spectrum extends up to a frequency above which the jet is no longer self-absorbed, and the jet spectrum breaks. At this spectral break frequency (typically at IR frequencies during the beginning of the outburst; Russell et al. 2013a), the optically thick synchrotron spectrum transitions to a steep optically thin spectrum ($\alpha \approx -0.7$; Corbel & Fender 2002; Russell et al. 2013a). The frequency of this break is related to the

distance between the BH and the location where nonthermal particles are first accelerated in the jet (e.g., Markoff et al. 2001, 2005; Romero et al. 2017; Ceccobello et al. 2018), where higher frequencies lie closer to the central compact object.

As the outburst progresses, the accretion rate increases and the X-ray and radio emission continue to brighten. The X-ray spectrum softens as it becomes increasingly dominated by softer (multi-temperature) blackbody emission arising from a geometrically thin disk. During this softening, the X-ray spectral and variability properties change as the system transits through the hard (HIMS) and soft (SIMS) intermediate states as it moves toward the soft state.

The transition from the HIMS to the SIMS is typically marked by a rapid decrease in the fractional rms variability of the X-ray emission and the transition between two types of quasi-periodic oscillations (QPOs), type-C and type-B QPOs, respectively (e.g., Wijnands et al. 1999; Homan et al. 2001; Remillard et al. 2002, see Casella et al. 2005 and Belloni 2010 for reviews). At some point during this progression, the jet properties change significantly. The steady, compact jet switches off (being quenched by at least 2.5 orders of magnitude in the radio band; Russell et al. 2011), as the jet spectral break evolves to lower frequencies (through the radio band; e.g., Corbel et al. 2013b; Russell et al. 2013b, 2014). The transient jet is launched during this phase. The radio emission from this jet is characterized by bright radio flares (e.g., Tetarenko et al. 2017b) that exhibit a steep radio spectrum (e.g., Fender 2001), thought to originate from ejected (optically thin) synchrotron emitting plasma that collides either with the preexisting and slower-moving jet, giving rise to internal shocks (e.g., Jamil et al. 2010), or with the surrounding environment. However, the sequence of the changes in the properties of the accretion flow and jet is currently poorly understood.

The transient jet is composed of discrete, bright, relativistically moving knots/ejecta that move outwards, away from the compact object (e.g., Corbel et al. 2004; Fender et al. 2004). To date, these discrete ejecta have been directly resolved in only a handful of BH LMXB systems (e.g., Mirabel & Rodríguez 1994; Hjellming & Rupen 1995; Tingay et al. 1995; Fender et al. 1999; Mioduszewski et al. 2001; Yang et al. 2010; Miller-Jones et al. 2012a, 2019). The mechanism responsible for the launching of these discrete jet knots is not well understood. Attempts to link changes in the X-ray properties to the timing of the radio flares were not able to identify a clear signature (e.g., Fender et al. 2009; Tetarenko et al. 2017b). However, there is an expected, but unknown, delay between the launching time and subsequent radio flaring (due to travel time and optical depth effects, as well as the cadence of radio observations typically not detecting the immediate onset of the flare). This delay can be accounted for by tracking the motion of the knot away from the BH and extrapolating back in time to determine the true launching time (e.g., Fender et al. 2009; Miller-Jones et al. 2012a).

The source then transitions to the soft X-ray state, where the X-ray emission is dominated by a multi-temperature blackbody component, with a weak, steep power-law component. In the soft state, radio emission from the compact jet is not detected, although some radio emission may be detected from the transient jets as they move downstream and interact with the surrounding environment (e.g., Corbel et al. 2002, 2004; Rushton et al. 2017).

As the accretion rate decreases, the X-ray luminosity decreases and the source begins to spectrally harden. During the reverse transition through the intermediate states and back to the hard state, the compact jet gradually reestablishes itself. The jet is first detected at radio wavelengths, then in the millimeter and IR bands

(e.g., Miller-Jones et al. 2012b; Kalemci et al. 2013), as the jet spectral break shifts to higher frequencies (Russell et al. 2013b, 2014). Jet flaring is not observed during this reignition.¹⁷ The source then typically fades toward quiescence, as the outburst ends.

1.1. MAXI J1535–571

MAXI J1535–571 was first discovered going into outburst when it triggered the Monitor of All-sky X-ray Image (MAXI) Gas Slit Camera nova alert system (Negoro et al. 2010) and the *Neil Gehrels Swift Observatory* (*Swift*) Burst Alert Telescope (BAT) hard X-ray transient monitor (Krimm et al. 2013) on 2017 September 02 (MJD 57,998; Markwardt et al. 2017; Negoro et al. 2017a). Subsequent X-ray and optical follow-up observations localized the position of the source (Kennea et al. 2017; Scaringi & ASTR211 Students 2017a, 2017b). MAXI J1535–571 was identified as a BH candidate due to its X-ray (Negoro et al. 2017b) and radio (Russell et al. 2017) properties. Further follow-up observations at other wavelengths detected the counterpart in the IR (Dincer 2017) and millimeter (Tetarenko et al. 2017a) bands. From HI absorption, the source distance was estimated to be $4.1^{+0.6}_{-0.5}$ kpc (Chauhan et al. 2019).

After the end of its outburst, MAXI J1535–571 did not decay toward quiescence. Instead it exhibited multiple (>5), short (and progressively less luminous) X-ray re-brightenings (Lepingwell et al. 2018; Negoro et al. 2018; Parikh et al. 2018, 2019). During a few of these re-brightenings, the source transitioned between the hard and soft states, and radio emission was detected (see Parikh et al. 2019 for discussions of the radio and X-ray observations taken during the re-brightenings).

In this paper, we present comprehensive radio monitoring of MAXI J1535–571 during its outburst, showing the evolution of the jet. In particular, we discuss the quenching of the compact jet, as well as the launching of the transient jet over the hard-to-soft state transition. We track the motion of a discrete jet knot over 303 days, which allows us to place constraints on the time of its launching and the properties of the accretion flow at the time of the ejection. We also use the observed properties of the detected jet knot to place constraints on the inclination, speed, and opening angle of the jet at the time of the ejection.

While this work only discusses the radio and X-ray behavior during the major outburst (and not the re-brightenings), we present detections of the jet knot up to ~ 5 months after the end of the major outburst.

2. Observations

2.1. Australia Telescope Compact Array (ATCA) Radio Observations

We monitored the radio counterpart of MAXI J1535–571 with the ATCA during its 2017/2018 outburst (under project codes C2604 and C3057). Throughout the major outburst, we carried out observations on 37 epochs between MJD 58,001 (2017 September 05) and MJD 58,249 (2018 May 11). The ATCA observations were taken every 1–10 days during the initial hard state rise and transition to the soft state (MJDs 58,001–58,060), every 1–4 weeks throughout the soft state (MJDs 58,060–58,221), and every 1–10 days during the decay phase (MJDs 58,031–58,249).

¹⁷ Except in Cyg X-3, where radio flares during the soft-to-hard state transition are thought to arise when the reignited jet has to burrow its way through the channel that has been filled in by the winds from the Wolf-Rayet companion (Koljonen et al. 2010).

All observations were taken at central frequencies of either 5.5 and 9.0 GHz, 17.0 and 19.0 GHz, or at all four frequencies. Each frequency pair (either 5.5 and 9.0, or 17.0 and 19.0 GHz) was recorded simultaneously with a bandwidth of 2 GHz at each frequency. Primary flux calibration was done using either PKS 1934–638 or PKS 0823–500, depending on whether the preferred source, PKS 1934–638 was visible at the time of the observation. PKS 1520–58 was used for secondary phase calibration for all observations except those taken on MJDs 58,001 and 58,008 where 1511–55 was used. The data were edited for instrumental issues and radio frequency interference before being calibrated following standard routines¹⁸ in the Common Astronomy Software Application (CASA version 5.1.0; McMullin et al. 2007). Calibrated data were then imaged using CLEAN within CASA. The 5.5 GHz data were imaged with a robust parameter of 0 to minimize effects due to extended emission from a nearby ($\sim 180''$ away) source. All other frequencies were imaged with a robust parameter of 2 (natural weighting) to maximize the image sensitivity. Where possible (when MAXI J1535–571 was detected above $\gtrsim 10$ mJy), the data were self-calibrated (phase and amplitude) down to a solution interval of 10 s.

We determined the radio flux density (S_R) by fitting a point source in the image plane. All flux densities are reported in the Appendix and shown in Figure 1. The radio luminosity (L_R) was calculated by $L_R = 4\pi S_R \nu D^2$, where D is the source distance.

We measured the position of the jet knot, the core position of MAXI J1535–571 (hereafter, only referred to as MAXI J1535–571), and other objects in the field by fitting point sources in the uv-plane of the 9 GHz¹⁹ observations using UVMULTIFIT (Martí-Vidal et al. 2014). For each epoch, the positions of the target and jet knot were corrected using the positional offsets determined from a bright source in the field. All applied positional shifts were $< 0''.5$ in R.A. and $< 0''.8$ in decl., with both being typically $< 0''.2$. Measured flux densities and positions (as well as the telescope configuration) are presented in the Appendix tables.

2.1.1. Intra-observation Variability

UVMULTIFIT was also used to search for source variability within each epoch, where we fit for a point source in the uv-plane for different time intervals within each observation. Many of our radio observations were short in duration (generally only 15–30 minutes long), meaning that for many observational epochs the short time variability could not be well explored. Therefore, for most ATCA observations during the outburst we only observed small changes in the source flux density (by $\lesssim 3\%$) over the radio observation.

However, we detected source variability on three epochs, on MJDs 58,013, 58,017, and 58,019, where the source varied significantly when compared to other sources in the field. This variability is discussed in Section 3 and shown in Figures 2 and 3.

2.2. MeerKAT Radio Observation

The field surrounding MAXI J1535–571 was observed with the MeerKAT radio observatory (Jonas & MeerKAT Team 2016; Camilo et al. 2018) for 2.1 hr on MJD 58,222 (2018 April 14), as

part of the ThunderKAT Large Survey Project (Fender et al. 2017). The observation was recorded at a central frequency of 1.28 GHz with a bandwidth of 856 MHz split into 4096 channels, and an 8 s integration time. PKS 0408–658 was used for bandpass and flux calibration, while PKS 1421–490 was used for phase calibration.

The data were flagged using AOfLAGger²⁰ (version 2.9; Offringa 2010) and calibrated following standard procedures within CASA (version 5.1.0, McMullin et al. 2007). To reduce data volume the raw data was binned (8 channels per bin), resulting in 512 channels with a channel width of 1.67 MHz each. Imaging was then carried out with the new wide-band, wide-field imager, DDFacet (Tasse et al. 2018). DDFacet is based on a co-planar faceting scheme and takes into account generic direction-dependent effects that dominate wide fields (such as the $\sim 1^\circ$ field of view of MeerKAT). A Briggs robust parameter of 0 was used during imaging, and deconvolution was done over four frequency blocks using the SSDCLEAN deconvolution algorithm. DDFacet is accompanied by the calibration software killMS,²¹ which was used to self-calibrate the data in order to correct for artifacts from bright sources. The image quality was also optimized using the COHJONES (Complex Half-Jacobian Optimization for N-directional Estimation; Smirnov & Tasse 2015) algorithm, which solves for scalar Jones matrices in a user-defined number of directions and includes corrections for direction-dependent effects.

The position of the jet knot was measured before self-calibration using IMFIT within CASA. As described in Section 2.1, we corrected the position relative to the location of the same bright nearby source used for the 9 GHz ATCA data. The measured flux density and position are given in the Appendix.

2.3. X-Ray Observations

MAXI J1535–571 was well monitored in the X-ray band throughout its major outburst. The *Swift*-X-ray telescope (XRT) monitored MAXI J1535–571 (target ID: 00010264) during the outburst rise and decay, MAXI observed MAXI J1535–571 intensively throughout the entire outburst, while HXMT (Huang et al. 2018) and AstroSAT (Sreehari et al. 2019; Bhargava et al. 2019) monitored the source densely for periods during the rise of the outburst.

For our comparison between the hard state radio (L_R) and X-ray (L_X) luminosities (Section 4.1.1), we analyzed ATCA observations of MAXI J1535–571 and *Swift*-XRT observations of MAXI J1535–571, respectively. This X-ray analysis is reported in full detail by Parikh et al. (2019), but we briefly summarize the analysis below.

All *Swift*-XRT data were downloaded from the HEASARC archive and processed using `xrtpipeline`. Pileup corrected *Swift*-XRT Windowed-timing mode observations were extracted in the 0.7–10 keV range and then fit using the X-ray spectral fitting package (XSPEC, version 12.9.1; Arnaud 1996). The equivalent hydrogen column density (N_H) was modeled using WILM abundances (Wilms et al. 2000) with `tbabs` and `VERN` cross-sections (Verner et al. 1996). N_H was left as a free parameter, where the value used for the X-ray luminosities was the average, providing $N_H = 3.54 \pm 0.03 \times 10^{22} \text{ cm}^{-2}$. To determine the X-ray flux of MAXI J1535–571 at the time of the radio observations, the hard state data were modeled (and well fit) with a simple absorbed power-law model (`tbabsxpowerlaw`); the

¹⁸ Exempli gratia, https://casaguides.nrao.edu/index.php/ATCA_Tutorials.

¹⁹ The 9 GHz observations provide the best balance between sensitivity, resolution, and phase stability. Position fitting was carried out before self-calibration.

²⁰ <https://sourceforge.net/projects/aoflagger/>

²¹ <https://github.com/saopicc/killms>

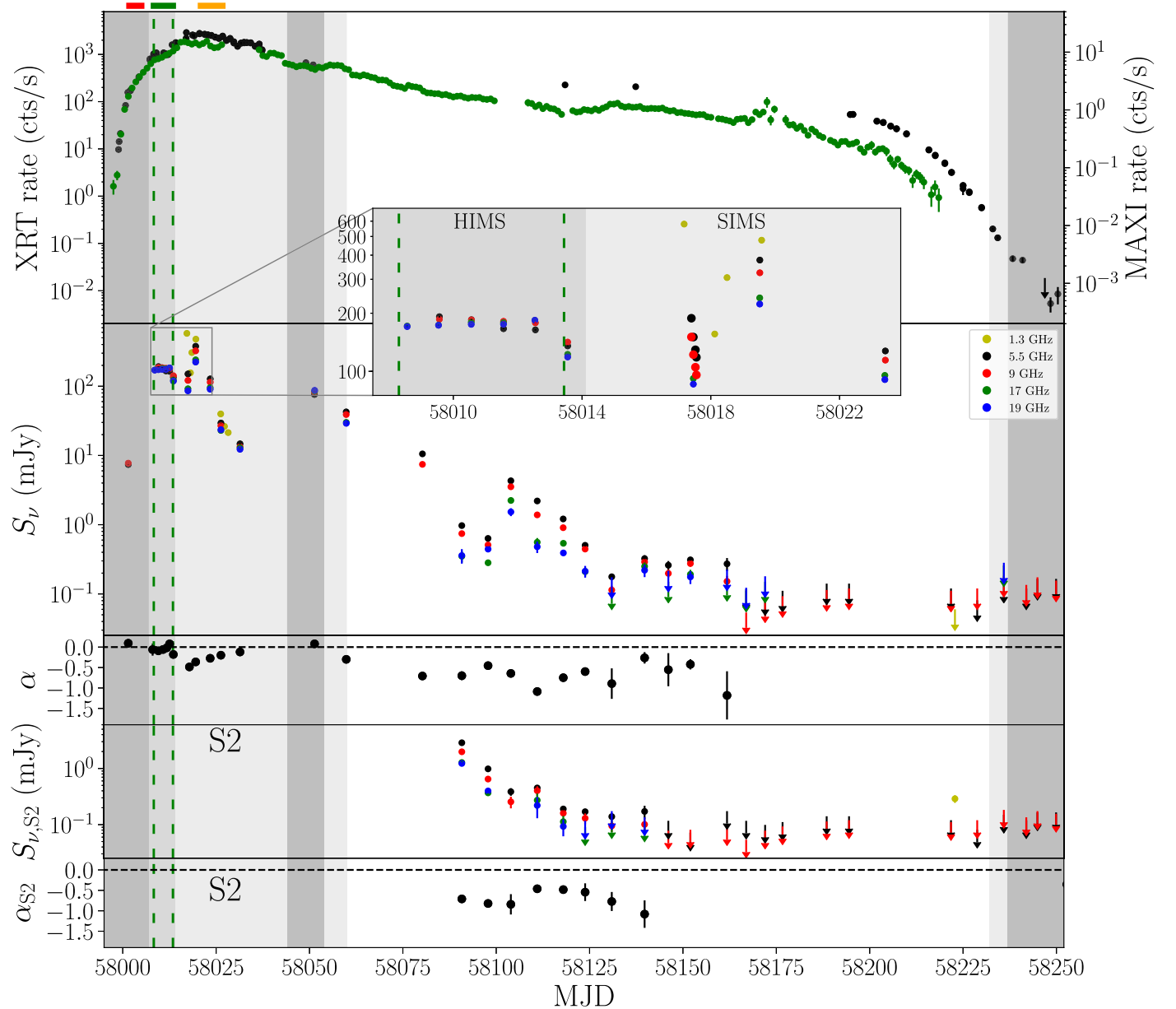


Figure 1. X-ray and radio light curves of MAXI J1535–571 during its 2017/2018 major outburst. *First panel:* Swift/XRT (left axis, black points) and MAXI (right axis, green points) light curve of MAXI J1535–571 throughout the outburst. *Second panel:* multifrequency radio monitoring of MAXI J1535–571. Also shown is a zoomed insert of the time range MJDs 58,008–58,023, highlighting the period of jet quenching and flaring. We include 1.34 GHz ASKAP data from (Chauhan et al. 2019) and the short time variability of our observation on MJD 58017.5 showing the fading radio emission from the first radio flare, see also Figure 2. *Third panel:* radio spectral index of MAXI J1535–571. *Fourth panel:* flux density measurements of the discrete jet knot, S2. *Fifth panel:* radio spectral index of S2. The dark shaded regions indicate when the source was in a hard state, the lighter shaded regions indicate the progressive intermediate states, where the darker is the HIMS and the lighter is the SIMS. The unshaded regions indicate the soft states (see Section 3.1 and Table 1 for the timing of the spectral state transitions). We show the extent of the modeled ejection dates at the top of the figure. Red represents the bulk motion model, orange is the decelerated motion model, and green shows the bulk plus decelerated motion model. The green vertical dashed lines show the most plausible ejection dates across all panels. All flux densities are provided in the Appendix. Here we show the evolution of the radio emission from MAXI J1535–571 and S2 during the major outburst.

1–10 keV X-ray de-absorbed flux (S_X) was then calculated using the XSPEC convolution model `cflux` before being converted to a luminosity as $L_X = 4\pi S_X D^2$.

3. Results

X-ray and radio observations (Figure 1) show MAXI J1535–571 brightens and fades over its 2017/2018 outburst. During this outburst, the source evolved through the X-ray spectral states, producing significant changes in the observed X-ray and radio properties.

3.1. X-Ray Spectral State Evolution from the Literature

For the state transitions and general behavior, we adopt X-ray spectral results reported by Tao et al. (2018) based on the *Swift*-XRT monitoring. However, at times when *Swift* did not observe the source, we also refer to the behavior and state transitions reported from MAXI monitoring (Nakahira et al. 2018). The evolution is supported by timing results from HXMT monitoring (Huang et al. 2018). Table 1 summarizes the X-ray spectral state evolution of MAXI J1535–571 from these studies.

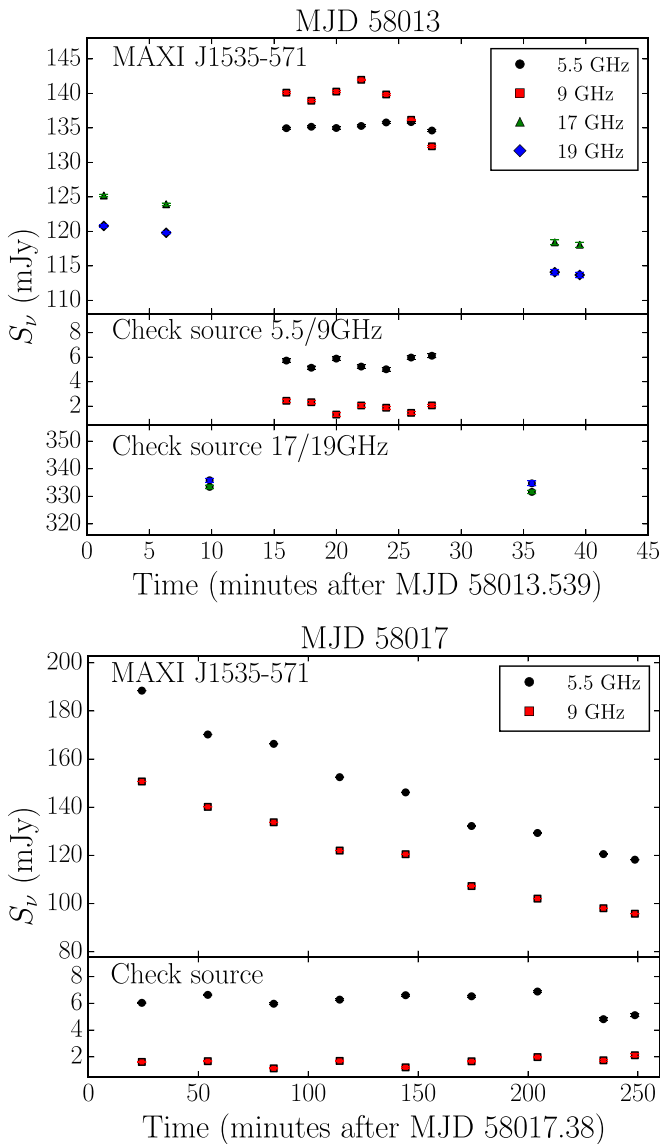


Figure 2. Intra-observation radio variability of MAXI J1535–571 during ATCA observations on MJD 58,013 (top figure) and MJD 58,017 (lower), when the source was in the HIMS and SIMS, respectively. These light curves highlight the radio variability of the target. We also show the radio emission from a check source within the field at 5.5 and 9 GHz, and treat two phase calibrator scans as a target/check source at 17 and 19 GHz (there was no nearby check source at 17 and 19 GHz) to show that the variability is intrinsic to MAXI J1535–571. The variability on MJD 58,013 implies the beginnings of jet quenching as the jet spectrum changes. The fading emission on MJD 58,017 indicates the end of the first radio flare.

3.2. Radio Results

Throughout its outburst, we detected radio emission from MAXI J1535–571 that was consistent with either a steady, compact jet or a flaring, transient jet (identified by the flat-to-inverted, or steep radio spectrum, respectively). We also monitored a downstream radio knot from the transient jet that was spatially resolved from MAXI J1535–571 and moving away. We refer to this discrete knot as S2 hereafter. For clarity, in the results section we present the results from each of these two components separately. Section 3.3 describes the radio emission that was spatially coincident with MAXI J1535–571, regardless of whether it originated from the compact or transient jet. Section 3.4 presents the emission from S2.

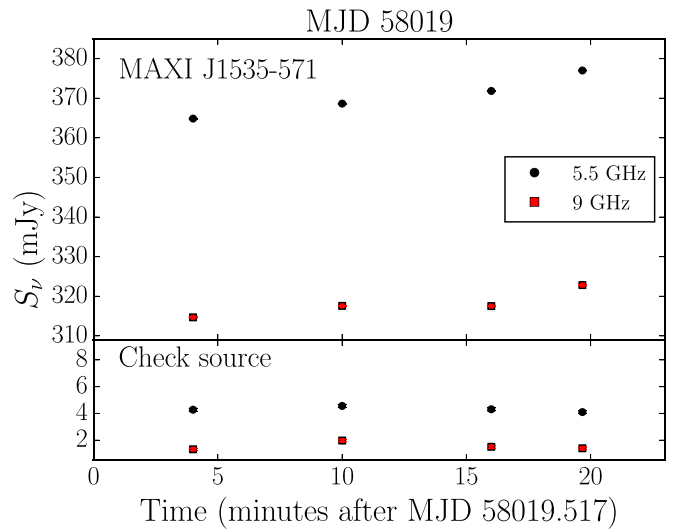


Figure 3. Intra-observation radio variability of MAXI J1535–571 (in the SIMS) during ATCA observations on MJD 58,019. Here we show the rising radio emission from MAXI J1535–571 during the second radio flare (top panel). We also show the nonvariable radio emission from a check source within the field (lower panel).

Table 1

Tabulated X-Ray Spectral State Evolution of MAXI J1535–571 during its 2017/2018 Major Outburst

MJD	X-ray State Transition
58,004.49 ^a –58,007.27 ^a	Hard state → HIMS
58,014.18 ^a –58,015.37 ^a	HIMS → SIMS
58,044 ^b	IMS → hard state
58,054 ^b	Hard state → IMS
58,060 ^b	IMS → soft state
58,233 ^a	Soft state → IMS
58,237 ^a	IMS → hard state

Notes. The X-ray spectral evolution is from *Swift*-XRT monitoring (Tao et al. 2018) and MAXI (Nakahira et al. 2018). HIMS and SIMS denote the hard and soft intermediate state, while IMS is the intermediate state from the MAXI monitoring, which does not clearly distinguish between the HIMS and SIMS.

^a From (Tao et al. 2018).

^b From (Nakahira et al. 2018).

3.3. Radio Emission from the Location of MAXI J1535–571

Following the initial MAXI and *Swift*/BAT detections on MJD 57,998 (Markwardt et al. 2017; Negoro et al. 2017a), we observed MAXI J1535–571 with ATCA on MJD 58,001, as it brightened during the hard X-ray state. These ATCA radio observations significantly detected the radio counterpart of MAXI J1535–571 at an R.A. and decl. of:

$$\text{R.A. (J2000)} = 15^{\text{h}}35^{\text{m}}19^{\text{s}}.71 \pm 0.08$$

$$\text{Decl. (J2000)} = -57^{\circ}13'47''.58 \pm 0.06,$$

where the errors presented are the estimated systematics (as a distance from the phase calibrator) added in quadrature with the statistical errors on the fit (which are larger than the theoretical error of beam centroiding, $\text{beam}/2 \times S/N$).

3.3.1. Radio Light Curves and Spectra

Following our initial radio detection on MJD 58,001, MAXI J1535–571 brightened at both radio and X-ray wavelengths

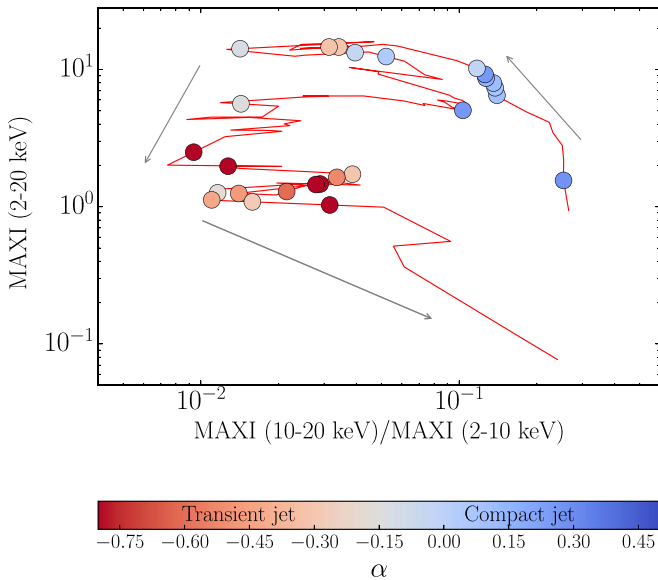


Figure 4. Hardness intensity diagram (HID) of MAXI J1535–571 during its major outburst, where the hardness was determined from MAXI data. For clarity, we only show MAXI detections greater than 1.5σ . Gray arrows indicate the overall evolution. The timing and spectral index, α , of the radio observations are shown by the overlaid circles, where the blue represents a flat-to-inverted radio spectrum (compact jet), and red represents a steep radio spectrum (from the transient jet), as indicated by the color bar. We see the compact jet evolve to the transient jet as the source underwent rapid X-ray spectral softening. The compact jet recovered during a brief return to the hard state before rapid softening once again (as the radio spectrum became steep).

over the next \sim week as the X-ray spectrum slowly softened (Figure 4), although the source remained in the HIMS. After this phase of rapid radio brightening, the radio emission then remained relatively steady ($S_{5.5 \text{ GHz}} \approx 170\text{--}180 \text{ mJy}$) from \sim MJD 58,008.5 until MJD 58,012.5 (during which we observed daily; Figure 1). Over this time, although the radio spectrum evolved marginally, the spectral index generally remained flat to inverted, indicating the continued presence of the compact jet.

Our final ATCA observation within the HIMS (starting \approx MJD 58,013.5) showed that the radio emission as a whole had faded ($S_{5.5 \text{ GHz}} \approx 135 \text{ mJy}$) and the radio spectrum had steepened while the X-ray luminosity increased (Figure 1). This epoch is a little more complicated than just steady fading and shows strong evidence that the jet spectral break had moved into, and through, the radio band during this epoch. The evolution of the jet spectral break will be discussed in greater detail in T. D. Russell et al. (in preparation), however, we summarize the behavior during this epoch here. This evidence is highlighted by the radio spectrum initially remaining \sim flat (-to inverted) between the 5.5 and 9 GHz ATCA bands, while the 17–19 GHz emission was fainter than the lower-frequency observing bands (and continuing to fade²²) and exhibited a steep radio spectrum (Figure 2, top). Toward the end of the observation, the 5.5 and 9 GHz radio spectrum also steepened due to rapid fading at 9 GHz. This evolution implies that the jet spectral break resided within the radio band during this observation. Such behavior indicates the beginning of the

quenching of the radio jet, which is supported by a sharp drop in the IR and optical brightness between MJDs 58,012 and 58,016 (Baglio et al. 2018).

Our next radio observation (\approx MJD 58,017.4) occurred within the SIMS. Dividing that radio observation into 2-minute time intervals showed that MAXI J1535–571 was brighter ($S_{5.5 \text{ GHz}} \approx 190 \text{ mJy}$) at the beginning of that observation, with the radio emission fading steadily at all frequencies (to $S_{5.5 \text{ GHz}} \approx 118 \text{ mJy}$; Figures 1 and 2) during the \approx 3.5 hr radio observation. At all times the radio spectrum was steep ($\alpha \approx -0.5$). Additionally, the Australian Square Kilometre Array Pathfinder (ASKAP) also detected a bright radio peak (\approx 580 mJy) in the 1.4 GHz light curve \sim MJD 58,017.17 (Chauhan et al. 2019), which are included in Figure 1. These results indicate that a bright radio flare occurred between MJDs 58,013.5 and 58,017.4.

A second bright, steep-spectrum radio flare was observed to be rising during our radio observation on MJD 58,019 (Figure 3). This second flare then faded over the next few weeks. However, instead of continuing to fade, MAXI J1535–571 temporarily returned back to a hard state between MJDs 58,044 and 58,054. During this period the radio jet re-brightened and the radio spectrum was observed to be flat (Figure 1).

After this brief return to the hard state, MAXI J1535–571 entered the soft state and faded slowly in the X-ray band over the next \sim 160 days. During this steady soft-state decay, we continued to detect radio emission (with generally decreasing flux density and a steep radio spectrum) until MJD 58,161, more than 100 days after the hard-to-soft state transition. Throughout this evolution, we observed some minor radio flaring and changes to the radio spectrum (although α was always <0), indicating that the emission originated from a transient jet.

During the decay period at the end of the major outburst, we did not detect radio emission from the source. Of particular interest, during and after the soft-to-hard state transition (MJD 58,237) at the end of the outburst, we detected no radio emission from the source down to 3σ upper limits of $\approx 120 \mu\text{Jy beam}^{-1}$.

3.4. Radio Emission Associated with the Resolved Jet Knot, S2

ATCA observations taken on MJD 58,090 (2017 December 03) showed a second ($\sim 3 \text{ mJy}$) radio source (S2) located $\approx 5''$ to the southeast of the measured position of MAXI J1535–571 (Figure 5, middle panel). No counter-jet component was detected.

Imaging and uv-plane analysis for all observations prior to the detection on MJD 58,090 did not appear to show any detectable emission significantly offset from the position of MAXI J1535–571. In most cases it is not surprising that S2 (or a counter-component) was not spatially resolved in these earlier observations due to the poor spatial resolution (arising from the compact, H168, telescope configuration providing a spatial resolution of $\sim 160''$ at 5.5 GHz at those times). However, in early 2017 November, ATCA moved back to its extended 6 km array configuration, providing spatial resolutions of $\sim 1''\text{--}5''$. Using the proper motion we measured for S2 (Table 2), it would only have reached angular separations of a few arcseconds $\sim 50\text{--}100$ days after the ejection event occurred. Our two ATCA observations taken during 2017 November (on MJDs 58,059 and 58,080) may have been taken when S2 had traveled sufficiently far from MAXI J1535–571, but S2 was not detected in those observations (Figure 5). On MJD 58,059, the lack of detection could be due to S2 still being too nearby to

²² The 17 and 19 GHz bands were not observed simultaneously with the 5.5 and 9 GHz bands. Additionally, there was no nearby check source detected at 17 and 19 GHz, so the intrinsic variability check was done by treating the inner scans of the phase calibrator as a target source, while the other scans were used as the calibrator.

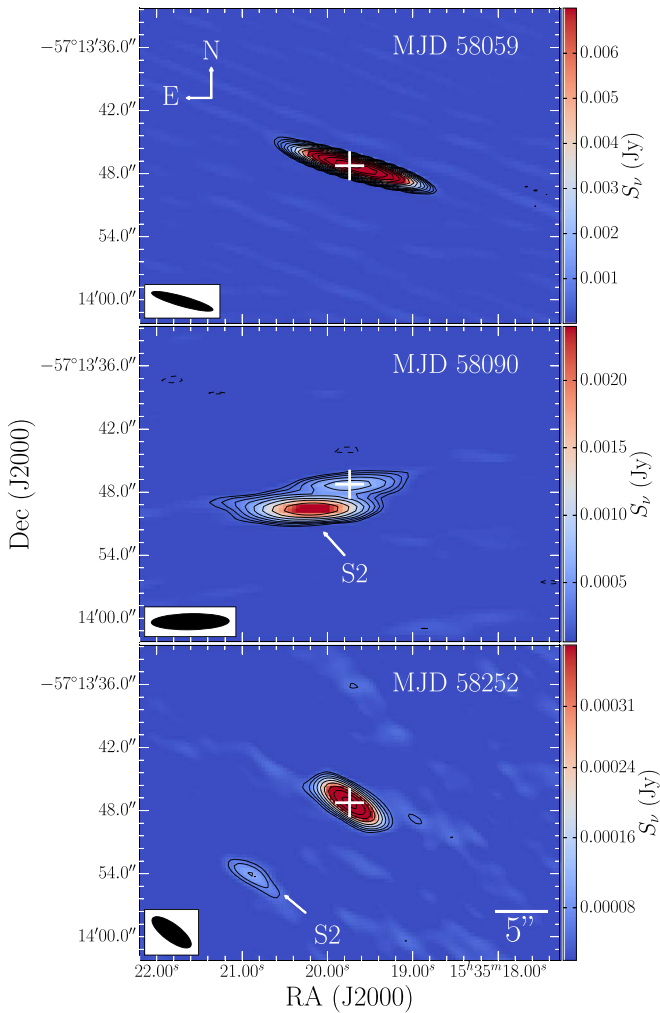


Figure 5. A sample of the 5.5 GHz ATCA monitoring of MAXI J1535–571 and S2, showing the motion of the S2 as it moved away from the source. The *top panel* shows non-detection of S2 on MJD 58,059, just after the telescope reconfiguration, the *second panel* shows our initial detection of S2, while the *third panel* shows the detection of S2 at much later times. This sample of images highlights the motion of S2 as it moved away from MAXI J1535–571 (where the source position is marked by the white cross in each image). Contours are $\pm\sqrt{2}^n$ times the rms, where $n = 3, 4, 5, 6, \dots$ and the rms was 60, 50, and $18 \mu\text{Jy beam}^{-1}$, respectively. Dashed contours represent negative values. S2 traveled away from MAXI J1535–571 at a position angle of $124^\circ.7 \pm 0^\circ.5$ east of north. S2 was detected over 12 observing epochs in total (see Table 4 and Figures 1 and 6).

MAXI J1535–571 for it to be spatially resolved, while our observation on MJD 58,080 only comprised 2×10 minutes on-source scans over a ~ 40 minutes period, providing poor uv-coverage and a high noise level (an rms of $\sim 120 \text{ mJy beam}^{-1}$ at 5.5 GHz and $\sim 170 \text{ mJy beam}^{-1}$ at 9 GHz).

The radio spectrum of S2 remained optically thin for all detections (Figure 1, fifth panel), and S2 was detected during all ATCA observations over the next ~ 2 months, and then sporadically by ATCA over a ~ 1 yr period, as well as during the single MeerKAT observation on MJD 58,222 (Figure 1 and Table 4). We observed S2 moving away from MAXI J1535–571 at a position angle of $124^\circ.7 \pm 0^\circ.5$ east of north, under the standard assumption of a ballistic (linear) trajectory.

From its motion and radio spectrum, S2 was consistent with emission from synchrotron emitting plasma, arising from

shocks or interactions by a discrete jet knot that was launched from, and subsequently moved away from, MAXI J1535–571. At no time was S2 observed to be extended or was another ejected component detected, either traveling in the opposite direction from the target (to the northwest of MAXI J1535–571) or in the same direction as S2 but at a different separation.

S2 faded steadily following its initial detection (Figure 1), dropping below our detection threshold of ~ 50 days after its initial identification (on MJD 58,090). Over this time, the radio spectrum remained steep, although it did vary.

During our continued monitoring of MAXI J1535–571 (during the reflares the source displayed after the major outburst ended), two additional brightenings of S2 were detected, allowing its motion away from the BH to be tracked over a period of 303 days during our monitoring.

To fit the motion of S2 we use a Markov chain Monte Carlo (MCMC) algorithm (EMCEE; Foreman-Mackey et al. 2013), where the best-fit result is taken as the median of the one-dimensional posterior distributions, and the uncertainties are reported as the range between the median and the 15th percentile (–ve), and the 85th percentile and the median (+ve), corresponding approximately to 1σ errors. Results from the MCMC fitting are reported in Table 2 and shown in Figure 6. We show the parameter correlations in the Appendix figures, which show no bimodal posterior distributions. We note that the small decrease we measure in the separation of S2 from MAXI J1535–571 on MJD 58,103 (Figure 6) likely arises from poor uv-coverage due to the short observation length resulting in unaccounted for systematics for that epoch.

While the majority of our monitoring appears to show S2 moving away from MAXI J1535–571 linearly in time (i.e., with a constant velocity; Figure 6), the final measured position seems to have not traveled as far as expected. This implies S2 decelerated over time, either for all times following its ejection, or just at later times. Therefore, we model the proper motion of S2 in three different ways. In the first case, we assume S2 traveled with a constant bulk motion (constant velocity). For the second case, we include an acceleration component in our model, allowing S2 to decelerate from the moment of launching. In the third case, we combined these two scenarios; where S2 initially traveled with a constant velocity until a time, t_{decel} , following which, S2 could decelerate. Such late-time deceleration could occur due to interactions with the interstellar matter (ISM), the preexisting jet, or once the knot had swept up enough mass to slow itself (see Section 4.2 for further discussion).

For the case of constant motion, we describe the motion of S2 away from the source as:

$$\begin{aligned} \text{R.A.}_{\text{offset}} &= \mu_{\text{R.A.}}(t - t_{\text{ej,bulk}}), \\ \text{Decl.}_{\text{offset}} &= \mu_{\text{Decl.}}(t - t_{\text{ej,bulk}}), \end{aligned} \quad (1)$$

where $\text{R.A.}_{\text{offset}}$ and $\text{Decl.}_{\text{offset}}$ correspond to the positional offset from the location of MAXI J1535–571 in R.A. and decl., respectively, $\mu_{\text{R.A.}}$ and $\mu_{\text{decl.}}$ are the proper motions in mas day^{-1} , t is the time (in MJD), and $t_{\text{ej,bulk}}$ is the time of zero separation between S2 and the source (time of ejection). Fitting all data points without any weighting determines the time of ejection, $t_{\text{ej,bulk}}$, to be $\text{MJD } 58,003.4_{-1.7}^{+1.6}$. Full results are shown in Table 2.

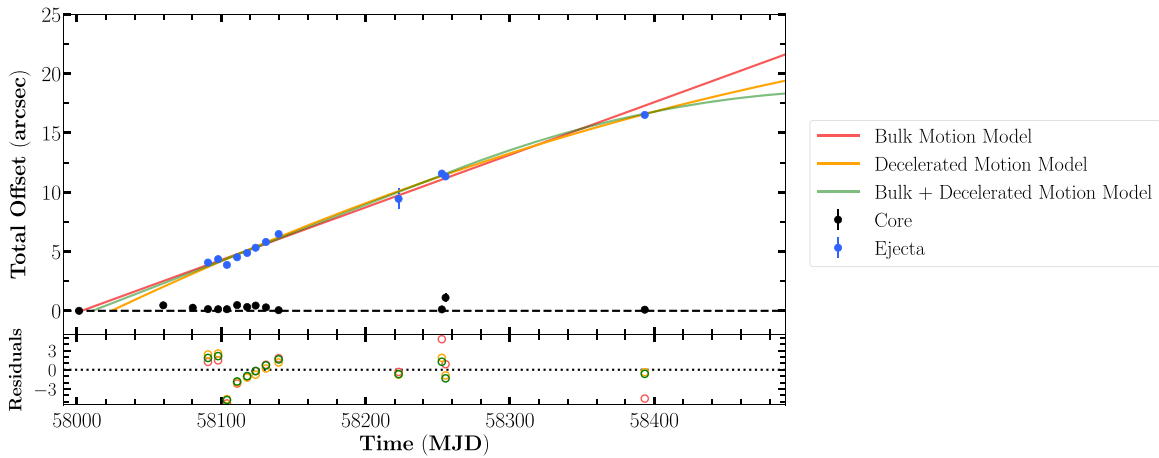


Figure 6. The separation (in arcseconds) over time of S2 (blue points) from MAXI J1535–571 (black points). Here, both sources have been normalized to the radio position of MAXI J1535–571 and corrected relative to another bright radio source in the field. We modeled the motion of the S2 with an MCMC algorithm using a constant bulk motion model (red line), a simple decelerating motion model (orange line), and a combination of the two, where S2 initially traveled with a constant velocity, before decelerating at later times. Residuals are shown in the lower panel, which were calculated as the data minus the model divided by the observational uncertainties. Extrapolating the motion of the knot back in time, these models estimate the time of zero separation between the core and knot (time of launching) to be MJD $58,003.4^{+1.6}_{-1.7}$, MJD $58,024.1^{+2.6}_{-3.2}$, or MJD $58,010.8^{+2.65}_{-2.5}$, respectively. Full model results are shown in Table 2.

Table 2
MCMC Modeling of the Proper Motion of S2

	$\bar{\mu}_{\alpha}$ (mas day $^{-1}$)	$\bar{\mu}_{\delta}$ (mas day $^{-1}$)	t_{decel} (MJD)	$\dot{\mu}_{\alpha}$ (mas day $^{-2}$)	$\dot{\mu}_{\delta}$ (mas day $^{-2}$)	μ_{ave} (mas day $^{-1}$)	t_{ej} (MJD)
Bulk motion	36.4 ± 0.4	$-25.35^{+0.25}_{-0.31}$	$44.37^{+0.6}_{-0.8}$	$58003.4^{+1.6}_{-1.7}$
Decelerating motion	$46.57^{+1.67}_{-1.83}$	$-34.0^{+1.2}_{-1.3}$...	0.05 ± 0.01	-0.05 ± 0.01	57.6 ± 3.0	$58024.1^{+2.6}_{-3.2}$
Combination (bulk+decel)	$38.7^{+1.0}_{-0.7}$	$-27.0^{+0.4}_{-0.7}$	58262^{+32}_{-65}	$0.11^{+0.08}_{-0.04}$	$-0.13^{+0.06}_{-0.09}$	47.2 ± 1.5	$58010.8^{+2.65}_{-2.5}$

Note. Here we use a bulk motion model (Equation (1)), a decelerating motion model (Equation (2)), or a combination of the two. For both R.A. and decl., we show the average proper motion as $\bar{\mu}_{\alpha}$ and $\bar{\mu}_{\delta}$, respectively. We also show the average acceleration in both R.A. and decl. ($\dot{\mu}_{\alpha}$ and $\dot{\mu}_{\delta}$, respectively), the average proper motion μ_{ave} , the deceleration start date t_{decel} for the combination model), as well as the best-fit date of the ejection (t_{ej}) in MJD.

Including constant deceleration at all times, we describe the motion away from the source as:

$$\begin{aligned} \text{R.A.}_{\text{offset}} &= \mu_{\text{R.A.}}(t - t_{\text{ej,decel}}) - \frac{1}{2}\dot{\mu}_{\text{R.A.}}(t - t_{\text{ej,decel}})^2, \\ \text{Decl.}_{\text{offset}} &= \mu_{\text{Decl.}}(t - t_{\text{ej,decel}}) - \frac{1}{2}\dot{\mu}_{\text{Decl.}}(t - t_{\text{ej,decel}})^2, \end{aligned} \quad (2)$$

where the variables are the same as those in Equation (1), except $\dot{\mu}_{\text{R.A.}}$ and $\dot{\mu}_{\text{Decl.}}$ are the R.A. and decl. acceleration terms (in units of mas day $^{-2}$). Using Equation (2), the time of zero separation is estimated to be $t_{\text{ej,decel}} = \text{MJD } 58,024.1^{+2.6}_{-3.2}$.

In the third case, we use a combination of the previous two models. Here, S2 can initially travel with a constant motion (described by Equation (1)) until time = t_{decel} , following which, S2 can decelerate (Equation (2)). This estimates the time of ejection to be $t_{\text{ej,comb}} = \text{MJD } 58,010.8^{+2.65}_{-2.5}$ and the time of deceleration to occur at $t_{\text{decel}} = \text{MJD } 58,262^{+32}_{-65}$.

We then compare these results (from Table 2) with the X-ray and radio monitoring to determine the most plausible scenario (Figure 1). Assuming simple bulk motion implies t_{ej} would have occurred early in the outburst, during the hard state when the source was brightening (Figure 7). This ejection window is well before the expected time for a jet ejection, which is typically believed to occur close in time to the transition to the SIMS or soft state (e.g., Corbel et al. 2004; Fender et al. 2004, 2009;

Miller-Jones et al. 2012a). Additionally, over this time we observe the brightening and then steady emission from the compact jet. The launching window is also ≈ 10 days prior to the onset of jet quenching in the radio band, with compact emission detected in the IR (Baglio et al. 2018) and millimeter (Tetarenko et al. 2017a), indicating the presence of the compact jet even at high energies (closer to the BH).

When deceleration was included for all times since the ejection (Equation (2)), $t_{\text{ej,decel}}$ was estimated to occur at a time when the X-ray emission was fading, and the source was undergoing spectral hardening (as it moved back toward a hard state; Figure 7). Additionally, this ejection date is >4 days after the end of the initial radio flare (Figure 2), and >1.6 days after we see rising radio emission indicating the second radio flare had already started (Figure 3). Given that a radio flare is caused by the ejected material moving away from the BH (to distances probed by the radio band), the flares should occur after the ejection event and not before. Hence, we also deem this scenario to be improbable.

Therefore, the most plausible scenario is the combination of the two models, where S2 traveled with an \approx constant velocity for the first ~ 260 days, before slowing as it interacted with a denser region of the jet or surrounding environment, or once it had swept up enough ISM to be equal to its own mass. This model places the launching time close to the HIMS-to-SIMS transition (see Section 4.2.2 for further discussion).

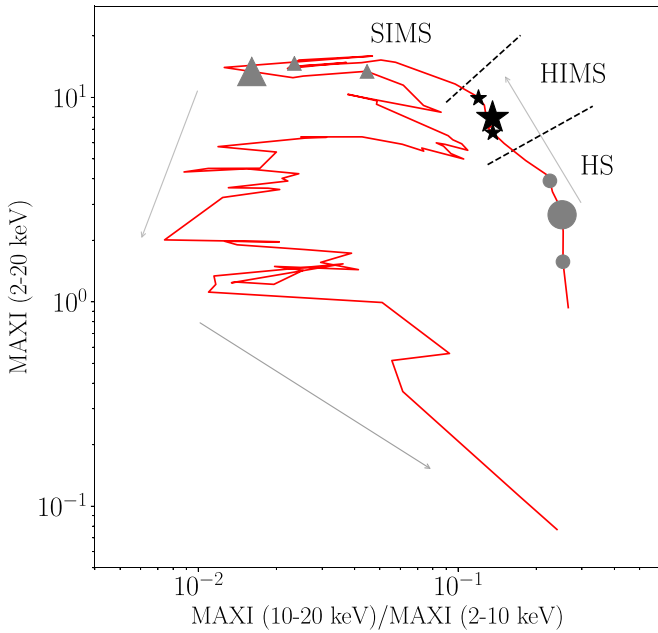


Figure 7. HID of MAXI J1535–571 during its major outburst (see Figure 4 for full details). Here, the black stars represent the best-fit ejection time, assuming S2 initially traveled with a constant motion before decelerating. The largest marker represents the best fit, while the smaller show the extent of the 1σ errors. We also show the estimated ejection times when we assume constant motion (gray circles), as well as allowing S2 to decelerate at all times (gray triangles). We mark the state transitions during the rise of the outburst (dashed lines) and the arrows indicate how the source evolved with time. The determined timing of the ejection event in comparison to the source evolution implies that the constant motion plus deceleration model best describes the data.

4. Discussion

4.1. The Evolving Radio Jet

Our multifrequency radio observations of MAXI J1535–571 show the evolution of the jet throughout its 2017/2018 major outburst. These observations probed the initial brightening of the compact radio jet during the hard state, the subsequent quenching of the compact jet, and radio flaring as the source moved through the intermediate states into the soft state. Our ATCA monitoring detected the re-appearance of the compact jet during a short-lived return to the hard state. We did not detect radio emission from the jet as it reestablished over the hard-to-soft return state transition at the end of this major outburst.

Additionally, over a period of nearly a year, ATCA and MeerKAT observations traced a spatially resolved downstream jet knot S2 as it moved away from the BH, allowing for constraints on the properties of the jet at the time of the ejection.

4.1.1. Hard State Radio/X-Ray Correlation

In their hard states, BH XRBs exhibit an empirical correlation between their radio (L_R) and X-ray (L_X) luminosities, which is observed over several orders of magnitude in luminosity (e.g., Corbel et al. 2000, 2003, 2013a; Gallo et al. 2003, 2012, 2018). This nonlinear relationship is generally described by two power-law tracks: an upper “radio-loud” track with a slope of $L_R \propto L_X^{0.6}$, and a lower “radio-quiet” track with a slope of $L_R \propto L_X^{-1}$ (e.g., Coriat et al. 2011; Gallo et al. 2012), which show different radio spectral indices (Espinasse & Fender 2018). We note that

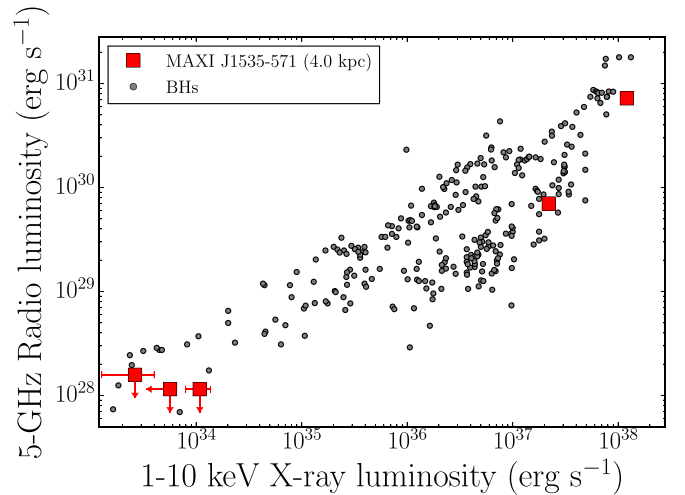


Figure 8. Hard state radio and X-ray measurements of MAXI J1535–571 during its major outburst (of which there were only two quasi-simultaneous hard state detections). We also show the (3σ) radio non-detections during the reverse transition at the end of the outburst. Here, the red squares show the luminosities for the estimated source distance of 4.1 kpc (Chauhan et al. 2019). The larger sample of BH systems are shown (from Corbel et al. 2013a; Bahramian et al. 2018). Our two contemporaneous hard state radio and X-ray detections suggest that MAXI J1535–571 lies on the radio-quiet track of the radio/X-ray correlation.

recent results have questioned the statistical significance of there being two separate tracks (Gallo et al. 2014, 2018).

We investigated the radio and X-ray relationship of MAXI J1535–571 by placing a contemporaneous hard state 5 GHz radio and 1–10 keV X-ray luminosities on the radio/X-ray plane (Figure 8). Unfortunately, due to the low cadence of our radio observations during the rising hard state, and the non-detection of radio emission following the transition back to the hard state at the end of the major outburst, we are only able to place two detections on the radio/X-ray correlation (with the upper limits showing the non-detection of the jet at the end of the outburst). From these two points, we determine a slope of $L_R \propto L_X^{1.37 \pm 0.05}$. However, while it appears that MAXI J1535–571 traced out the radio-quiet track, these two points only span 1 order of magnitude in L_R and a factor of ~ 6 in L_X , where previous studies (e.g., Corbel et al. 2013a) have shown significant deviation from a source’s standard behavior for luminosity ranges < 2 orders of magnitude.

4.1.2. Quenching of the Compact Jet

Following a period of relatively steady radio emission from the compact jet (\sim MJD 58,008 until MJD 58,012; Figure 1), we observed the initial stages of jet quenching. ATCA radio observations on MJD 58,013.5 showed that the radio emission had faded by a $\gtrsim 25\%$ (and was continuing to fade) and the jet spectral break had evolved into the radio band (Section 3.3.1, but will be discussed in detail by Russell et al. 2019, in preparation), driving the observed jet quenching (e.g., Fender et al. 1999; Coriat et al. 2011; van der Horst et al. 2013; Russell et al. 2013b, 2014).

The compact jet also re-formed during MAXI J1535–571’s brief return to the hard state, quenching once again as the source transitioned back to the soft state (through the intermediate states). This second quenching was also characterized by fading radio emission and a steepening radio spectrum.

The radio emission from MAXI J1535–571 faded below our detection limits on \sim MJD 58,166. Comparing our deepest soft-state radio upper-limit with the steady, flat-spectrum radio emission measured during the HIMS provides a lower-limit of >3.5 orders of magnitude on the jet quenching factor. This is the deepest constraint on the soft state jet quenching to date, suggesting that the compact jet was not present during this soft state (see also Fender et al. 1999; Coriat et al. 2011; Russell et al. 2011). However, our observations do not rule out jets with low-radiative efficiency in the soft states (Sikora et al. 2005; Drappeau et al. 2017), although see Koljonen et al. (2018) for evidence against a dark jet during the soft state in Cygnus X-3.

4.1.3. Reverse Transition at the End of the Outburst

At the end of its major outburst, MAXI J1535–571 transitioned from the soft to the hard state. This reverse transition was interesting for two reasons: (1) it occurred at a much lower X-ray luminosity than is generally expected, and (2) the radio jet was not detected.

In a typical BH XRB outburst, the hard-to-HIMS transition during the outburst rise occurs at an X-ray luminosity of $\geq 3\% L_{\text{Edd}}$, while the lower-luminosity transition back to the hard state at the end of an outburst occurs between 0.3% and 10% of L_{Edd} (Dunn et al. 2010; Kalemci et al. 2013; Vahdat Motlagh et al. 2019), with an average value of $\sim 2\%$ (Maccarone 2003). However, MAXI J1535–571 only transitioned back to the hard state at $L_X \sim 0.003\% L_{\text{Edd}}$ (see also Chauhan et al. 2019). Such low-luminosity transitions are atypical for BH XRBs, and the only other source to show similar behavior is 4U 1630–47, which transitioned from the soft-to-hard state at $L_X \approx 0.008\% L_{\text{Edd}}$ (Tomsick et al. 2014).

Low transition luminosities have been attributed to either the decay being disrupted by a new mass inflow reigniting and extending the soft state to a lower than usual X-ray luminosity (Vahdat Motlagh et al. 2019), or due to a low disk magnetic field and viscosity (e.g., Petrucci et al. 2008; Begelman & Armitage 2014).

For the case of a new mass inflow extending the soft state and pushing the reverse transition to much lower than typical luminosities, the jet may have been undetected due to the low transition luminosity. Assuming typical hard state L_R/L_X scalings (Figure 8), the X-ray luminosity over the reverse transition at the end of MAXI J1535–571’s outburst implies an expected radio flux density of $\sim 50\text{--}400 \mu\text{Jy}$. Therefore, while our 3σ radio upper limits are relatively radio faint in comparison with the majority of other hard state BHs, the radio non-detection is not remarkable.

In the case where low disk magnetic fields were responsible for the low-luminosity state transition, we may also expect weaker radio jets (e.g., Shibata & Uchida 1986; Kylafis et al. 2012; Begelman & Armitage 2014; Kylafis & Belloni 2015), resulting in the radio non-detection. Our data do not allow us to conclusively determine the cause of the low-luminosity transition or non-detection of the radio jets.

4.2. S2, an Apparently Superluminal Jet Knot

Our radio monitoring tracked the motion of the jet knot, S2, as it moved away from the core position of MAXI J1535–571 (Figures 5 and 6). We only detected a single-sided ejection. Assuming a bipolar ejection (e.g., Mirabel & Rodríguez 1994; Fender et al. 1999), the one-sided detection could be due to S2

being the approaching component, hence, the non-detection of a receding component could be due to Doppler boosting effects reducing the flux density as it receded (for details see e.g., Mioduszewski et al. 2001; Miller-Jones et al. 2011). Possible alternatives to explain the non-detection of a counter-jet component include absorption effects, lack of internal and external shocks (within the jet, or with the surrounding medium), optical depth effects, or asymmetries in jet launching (e.g., Hjellming & Rupen 1995; Fendt & Sheikhzadeh 2013).

Following its initial detection on MJD 58,090, S2 was detected in all radio observations until MJD 58,139 (over 40 days), when it dropped below our detection threshold. During these detections, S2 faded steadily (Figure 1), likely as it expanded adiabatically. However, S2 also re-brightened at later times, being detected during a MeerKAT observation on MJD 58,222, as well as consecutive ATCA observations on MJDs 58,252 and 58,255. S2 was again detected much later, during an ATCA observation on MJD 58,393, which was 303 days after its initial detection. While S2 was not detected during our monitoring on other dates before, between, and after these re-brightenings (see Table 4). As highlighted by the MeerKAT detection (at 1.3 GHz, which would translate to a 5.5 GHz flux density of $\sim 105 \mu\text{Jy}$) it is possible that S2 was below the ATCA detection threshold for some of these observations.

The re-brightenings of S2 at these later times could be produced by internal shocks with the preexisting jet or interactions with the ISM, where inhomogeneities can cause the multiple brightenings (e.g., Corbel et al. 2002, 2005; Kaaret et al. 2003; Migliori et al. 2017). Such interactions with the ISM could also lead to S2 decelerating at later times. Alternatively, the slowing may also have occurred once the S2 had swept up enough ISM material (equal to its own mass) to slow (e.g., Corbel et al. 2002).

4.2.1. Jet Knot Properties: Speed, Inclination, Opening Angle, Expansion, and Energetics

The proper motion of $47.2 \pm 1.5 \text{ mas day}^{-1}$ indicates an apparent jet velocity of $\approx 1.1 c$ for a source distance of 4.1 kpc. Apparent superluminal motions of jet ejecta have been observed in a handful of BH XRBs to date (e.g., Mirabel & Rodríguez 1994; Hjellming & Rupen 1995; Tingay et al. 1995; Rupen et al. 1998; Fender et al. 1999; Mirabel & Rodríguez 1999; Rodríguez & Mirabel 1999; Corbel et al. 2002; Fender et al. 2002, see Fender 2006, for review), and indicates that S2 was the approaching component.

Our tracking of S2 can be used to constrain the inclination of the jet (at the time of the ejection event; Miller-Jones et al. 2019) and the speed of the ejection. We did not detect a counter-jet component, so we cannot uniquely solve for the jet speed, $\beta = \frac{v}{c}$, or inclination, θ . Instead, we can only solve for $\beta \cos \theta$, given that (e.g., Rees 1966; Mirabel & Rodríguez 1994):

$$\mu_{\text{rec}}^{\text{app}} = \frac{\beta \sin \theta}{1 \mp \beta \cos \theta} \frac{c}{D}, \quad (3)$$

where μ_{app} and μ_{rec} are the approaching and receding proper motions, and D is the distance to the source. As shown in Figure 9, from its apparent superluminal motion, S2 is almost certainly the approaching component, with only a small set of solutions existing for it to be the receding component (only at

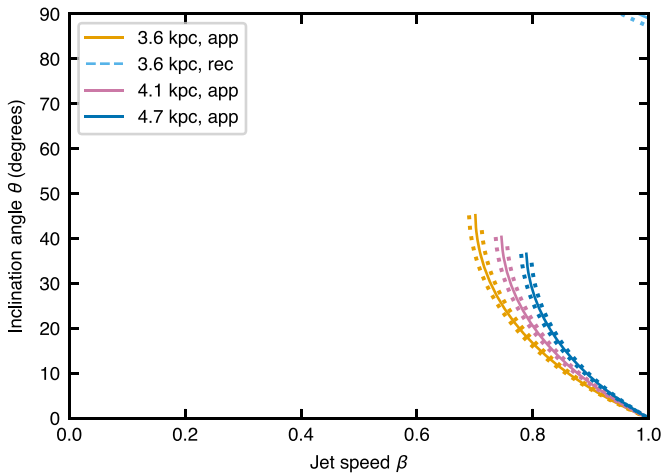


Figure 9. Constraints on the jet speed and inclination angle to the line of sight from the proper motion for the full range of source distances ($4.1^{+0.6}_{-0.5}$) presented by Chauhan et al. (2019). Uncertainties are shown as the dotted lines. For all but the lowest distance limit (of 3.6 kpc) S2 must be the approaching component.

the lowest distance limit; Chauhan et al. 2019), $\beta \cos \theta \geq 0.49$, such that $\beta \geq 0.69$ and $\theta \leq 45^\circ$.

X-ray spectral fits of the iron line during the HIMS (Miller et al. 2018; Xu et al. 2018) favored a disk inclination of $\sim 55^\circ$ – 68° , which is discrepant from our determined values for S2. However, there was some evidence for disk warping (Miller et al. 2018), suggesting that the inner disk orientation was changing over time. Such changes in the inner disk and jet orientation can be rapid (e.g., Liska et al. 2018; Miller-Jones et al. 2019), and would account for such a difference between the disk inclination and the jet when measured at different times. Additionally, the jet and outer disk may be misaligned.

S2 remained unresolved for all radio detections. Therefore, while we do not observe the expansion of S2, our observations can constrain the opening angle and transverse expansion of the jet from its width at a given distance from the core (e.g., Fender et al. 1999). Combining the $2''.9$ ATCA resolution with the $\sim 17''$ separation we measured when S2 was detected at its maximum separation, the jet opening angle is constrained to $\leq 10^\circ$, similar to typical constraints on BH XRB jet opening angles (see e.g., Miller-Jones et al. 2006). In terms of the transverse expansion, combining the ATCA beam size of our final detection with the ejection date, we limit the expansion velocity to $\leq 0.18c$, consistent with the expansion estimates found for V404 Cygni (Tetarenko et al. 2017b).

Using the proper motion of S2, we also estimate the size scale of the radio emission based on the delay between the ejection time and the time of the first radio flare. While we do not detect the peak of the first radio flare, we constrain it to have occurred between MJDs 58,013.6 and 58,017.4 (Section 3.3). Therefore, the \sim GHz radio emitting region lies at a distance of < 430 mas from the radio core. For a source distance of 4.1 kpc, this corresponds to a size of < 1760 au.

From the rise time and brightness reached by the second radio flare,²³ we also place constraints on the minimum energy and magnetic field required to produce such a flare. Following Fender (2006) and assuming equipartition between electrons

and magnetic field, and one proton per electron, we estimate the minimum energy $E_{\min} \sim 10^{42}$ – 10^{43} erg, corresponding to a minimum mean power $P_{\min} \sim 10^{37}$ erg s $^{-1}$ with an equipartition magnetic field, $B_{\text{eq}} \sim 10$ – 500 mGauss. These values are comparable to estimates from observed ejection events from a number of other sources (e.g., Fender et al. 1999; Brocksopp et al. 2007; Curran et al. 2014). Our energy estimates differ from the ejecta observed from V404 Cygni (Tetarenko et al. 2017b; Miller-Jones et al. 2019), however, in that outburst, multiple, smaller ejecta were observed, explaining the lower energies and higher magnetic fields.

4.2.2. X-Ray Properties at the Time of the Ejections

While there is a connection between the morphology of the jets and structure of the accretion flow (e.g., Fender et al. 2004), the causal sequence of events leading to the changes in the jets is not well understood, and the coupling is likely to be complex. The onset of the transient jet is generally linked to the transition from the HIMS to SIMS. The X-ray properties over this transition show a marked change (e.g., Belloni et al. 2005). For example, there is a sharp decrease in the fractional rms variability of the X-ray emission and the sudden appearance of a type-B QPO. It is these changes in the X-ray emission that have often been linked to the moment of an ejection event, in particular the presence of the type-B QPO (e.g., Fender 2006; Klein-Wolt & van der Klis 2008; Fender et al. 2009; Miller-Jones et al. 2012a). However, sparse observational sampling and the delay between an ejection and the observed radio flaring (due to optical depth effects and the time required for shocks to occur) generally prevents such a connection being clearly identified (see Fender et al. 2009, for a review).

During our radio coverage of the outburst of MAXI J1535–571, we observed the onset of the compact jet quenching in the radio band (which started \sim MJD 58,013.6). Our next radio observation (starting on MJD 58,017.4) detected the end of a radio flare. Therefore, this initial radio flare occurred between MJDs 58,013.6 and 58,017.4 and was likely associated with the ejection of S2, meaning that we would typically expect the ejection to have occurred at an earlier time (due to the time delay between an ejection event and the subsequent radio flaring; Fender et al. 2009).

Comparing our ejection window (between MJDs 58,008.3 and 58,013.4) to the X-ray properties produces interesting results. MAXI J1535–571 transitioned from the HIMS to SIMS sometime between MJDs 58,014.18 and 58,015.37 (Huang et al. 2018; Tao et al. 2018), close in time to the estimated ejection of S2. Huang et al. (2018) report a detection of a possible type-B QPO during HXMT observations taken on MJD 58015.97 (although this QPO was observed at a relatively high QPO frequency of ~ 10 Hz). While this QPO could be consistent with being close to the peak of the first radio flare (but certainly not before the beginning of the flare), it is after our t_{ej} window. In observations after this potential type-B QPO detection, only type-C QPOs were observed until MJD 58,017.5. HXMT and AstroSat observations taken during our ejection event window show high fractional X-ray variability ($\gtrsim 10\%$) with only the presence of type-C QPOs, with a changing QPO frequency (the QPO frequency first decreased, reaching a minimum \sim MJD 58,010, before increasing during the ejection window, although some scatter was observed; Huang et al. 2018; Bhargava et al. 2019; Sreehari et al. 2019).

Conveniently, the *Neutron Star Interior Composition Explorer (NICER)* X-ray telescope on board the International

²³ We did not adequately sample the first radio flare with our radio monitoring to estimate the radio brightness and rise time.

Space Station densely monitored MAXI J1535–571 around the time of the HIMS-to-SIMS transition (observing the source multiple times nearly every day). As reported by Stevens et al. (2018), the *NICER* X-ray observations also detected the appearance of a possible type-B QPO during observations starting on MJD 58,016.8, that remained until MJD 58,025 (but not during observations earlier and in particular, at similar times to when HXMT reported a type-B QPO). While this type-B QPO could be coincident with the second radio flare, it is not consistent with t_{ej} . Additionally, *NICER*'s high observing cadence showed the X-ray fractional variability was relatively high (dropping from $\approx 15\%$ to $\approx 11\%$) over our t_{ej} window, making it seem unlikely that a type-B QPO was present previously (typically, type-B QPOs occur at times of low fractional X-ray variability, $\approx 3\text{--}5\%$ rms; Belloni 2010).

The X-ray observations allow us to further investigate the X-ray properties at the time of t_{ej} . There was an initially steady drop in the X-ray rms variability (from $\approx 15\%$ to $\approx 11\%$ rms) between MJDs 58,011 and 58,014, followed by a more rapid decrease ($\approx 11\%$ to $\approx 7\%$ rms) between MJDs 58,013 and 58,015 (see Figure 1 in Stevens et al. 2018). Over this time, the X-ray observations also showed a steady drop in X-ray hardness, as well as an interesting and relatively sudden increase in the soft X-rays, where the count rate increased rapidly by a factor of ~ 2 between MJDs 58,010 and 58,014 (see Figure 1 in Stevens et al. 2018). While this increase could be due to a change in the accretion properties, similar short-high-energy brightenings are commonly associated to ejection events in active galactic nucleus (e.g., Marscher et al. 2008; King et al. 2016; Lisakov et al. 2017), where the X-ray increase can arise from inverse Compton scattering of the synchrotron radiation from the knot after it was ejected. If this X-ray increase was indeed related to the ejection of S2, it favors an ejection time of \sim MJD 58,010. Additionally, around the same time the QPO frequency rapidly decreased, reaching a local minimum \sim MJD 58,010 (after which it increased again; Huang et al. 2018; Sreehari et al. 2019). Speculatively, if the QPO frequency is related to the radius of the X-ray emitting material (e.g., Ingram et al. 2009), we may expect the QPO frequency to decrease due the extraction of accreting material in a jet ejection (Rapisarda et al. 2014). In addition, there was also a change in the QPO behavior at around MJD 58,013, when the QPO frequency varied rapidly (Bhargava et al. 2019).

Using high-resolution radio observations of the 2009 outburst of H1743–322, Miller-Jones et al. (2012b) were able track the motion of a bipolar ejection over two epochs, allowing tight constraints on the time of ejection (to within 1 day). While their estimated ejection date unfortunately coincided with a 3 day gap in X-ray monitoring, they determined that it occurred immediately prior to the HIMS-to-SIMS transition. Over this time, H1743–322 displayed a short increase (also by a factor of ~ 2) in the X-ray count rate, a rapid reduction in the X-ray rms variability, an evolution in the type-C QPOs, and the onset of compact jet quenching. Additionally, Miller-Jones et al. (2012b) only report the first appearance of a type-B QPO ~ 4 days after the estimated ejection event.

The similarities shown by H1743–322 and MAXI J1535–571 are striking. While in both cases we are unable to conclusively rule out the presence of a type-B QPO at the time of the jet ejection, the results suggest that, for these two outbursts, the X-ray signature of the ejection was not the

appearance of the type-B QPO. It could be that the jet ejection and type-B QPO are both a result of some other effect. Similar to findings reported by Miller-Jones et al. (2012b), our monitoring implies that the ejection event was instead related to the rapid drop in X-ray rms variability immediately prior to the HIMS-to-SIMS transition, the sudden increase in soft X-ray count rate, or the change in the type-C QPO frequency.

Fender et al. (2009) and Miller-Jones et al. (2012b) also compared outburst data from a number of other BH LMXBs, using either very long baseline interferometry data to trace ejecta back in time, or by connecting the timing of the radio flares to the X-ray behavior. Their analysis found no clear evidence of an association between the jet ejection and the appearance of type-B QPOs. In most cases, it appeared that the time of ejection was contemporaneous with a change in the type-C QPO and a decrease in the X-ray rms variability. However, as discussed by Fender et al. (2009) and Miller-Jones et al. (2012b), this did not hold true for all systems, or even outbursts from the same system. Radio and X-ray observations of the 2002 outburst of GX 339–4 showed that while the type-C QPO was changing at the time of the radio flare (Gallo et al. 2004; Belloni et al. 2005), the drop in X-ray rms variability was observed a few days after the radio flare (where the rms drop occurred at around the time of the detection of type-B QPO; Fender et al. 2009). Additionally, the 2003 outburst of H1743–322 did not appear to show an evolution of the type-C QPO during the estimated time of ejection (Miller-Jones et al. 2012b).

Therefore, while our MAXI J1535–571 results agree well with the 2009 outburst of H1743–322, as well as a number of other systems (as presented by Fender et al. 2009 and Miller-Jones et al. 2012b) comparisons with the 2002 outburst of GX 339–4 and 2003 outburst of H1743–322 muddy the picture. These two results imply that the events driving an ejection event may vary between systems and even outbursts of the same system. Alternatively, as discussed by Fender & Gallo (2014) there may be no clear X-ray signature to the moment of ejection, and the observed knots could be a result of internal shocks arising within the jets from rapid (but not instantaneous) changes in the injection, or speed of the jet-channeled accretion material (e.g., Jamil et al. 2010; Malzac 2013).

5. Conclusions

With our comprehensive radio monitoring of MAXI J1535–571 during its 2017/2018 major outburst, we have observed the evolution of the compact jet, as well as tracked the motion of a downstream jet knot.

Our observations constrain the compact jet quenching to be a factor of >3.5 orders of magnitude, implying that the compact jet was not visible during the soft state. Interestingly, the radio jet was undetected by our observations during the exceptionally low X-ray luminosity reverse (soft-to-hard state) transition at the end of the outburst, when we expect the compact jet to re-brighten.

From the observed radio flare and detection of the discrete, apparently superluminal jet knot, we place constraints on the properties of the jet. We estimate a jet opening angle of $<10^\circ$. We determine a jet inclination of $\leq 45^\circ$ at the time of ejection and a jet velocity of $\beta \geq 0.69$.

Extrapolating the motion of the knot back in time to determine the time of ejection reveals that in this outburst of MAXI J1535–571 the ejection likely occurred a few days

before the appearance of a possible type-B QPO in X-ray monitoring (which has often been associated with the transient jet launching). Instead, our results suggest that the ejection may be linked to the short increase in X-ray count rate, the observed drop in X-ray variability, or the change in the type-C QPO frequency, which was observed immediately before the HIMS-to-SIMS transition.

We thank the anonymous referee for their helpful comments. We thank Jamie Stevens and staff from the Australia Telescope National Facility (ATNF) for scheduling the ATCA radio observations. We also thank *Swift* for the scheduling of the X-ray observations. TDR thanks Abbie Stevens, Phil Uttley, and Craig Anderson for helpful discussions. T.D.R. acknowledges support from the Netherlands Organisation for Scientific Research (NWO) Veni Fellowship, Grant No. 639.041.646. A.J.T. is supported in part by a Natural Sciences and Engineering Research Council of Canada (NSERC) Post-Graduate Doctoral Scholarship (PGSD2-490318-2016). JCAM-J is the recipient of an Australian Research Council Future Fellowship (FT140101082), funded by the Australian government. G.R.S. and A.J.T. acknowledge support from an NSERC Discovery Grant (RGPIN-06569-2016). A.S.P. and R.W. are supported by a NWO Top grant, module 1, awarded to R.W. S.C. and E.T. acknowledge financial support from the UnivEarthS Labex program of Sorbonne Paris Cité (ANR-10-LABX-0023 and ANR-11-IDEX-0005-02). D.A. acknowledges support from the Royal Society. N.D. and J.v.d.E. are supported by a NWO Vidi grant, awarded to N.D. S.M. and M. L. are supported by a NWO Vici grant, awarded to S.M. (Grant

No. 639.043.513). P.A.W. acknowledges support from the NRF and UCT. This work was supported in part by the Oxford Hintze Centre for Astrophysical Surveys, which is funded through generous support from the Hintze Family Charitable Foundation. The International Centre for Radio Astronomy Research is a joint venture between Curtin University and the University of Western Australia, funded by the state government of Western Australia and the joint venture partners. The Australia Telescope Compact Array is part of the Australia Telescope, which is funded by the Commonwealth of Australia for operation as a National Facility managed by CSIRO. The MeerKAT telescope is operated by the South African Radio Astronomy Observatory, which is a facility of the National Research Foundation, an agency of the Department of Science and Technology. This research has made use of NASA's Astrophysics Data System.

Facilities: ATCA, *Swift*-XRT, MAXI.

Software: CASA, XSPEC, Astropy; (Astropy Collaboration et al. 2013).

Appendix Radio Data

Results from our radio monitoring campaign. Tables 3 and 4 provide the date, configuration, frequency, and flux density of MAXI J1535–571 and S2 for each ATCA and MeerKAT observation. Table 5 provides the positions of S2 from our best measured source position. We also include parameter correlation figures (Figures 10–12) for each of our fitted ejecta motion models.

Table 3
Radio Flux Densities of MAXI J1535–571

Start Date (UT)	MJD	Telescope ^a Configuration	Central Frequency (GHz)	Flux Density (mJy)	α
2017 Sep 05	58,001.48 ± 0.04	1.5A	5.5	7.39 ± 0.03	0.09 ± 0.02
			9.0	7.74 ± 0.05	
2017 Sep 12	58,008.57 ± 0.004	H168	17.0	171.69 ± 2.00	−0.06 ± 0.15
			19.0	170.52 ± 2.00	
2017 Sep 13	58,009.57 ± 0.01	H168	5.5	192.00 ± 1.80	−0.09 ± 0.01
			9.0	186.14 ± 1.00	
			17.0	173.72 ± 1.00	
			19.0	173.21 ± 1.00	
2017 Sep 14	58,010.563 ± 0.003	H168	5.5	185.30 ± 1.20	−0.06 ± 0.01
			9.0	184.73 ± 0.22	
			17.0	179.47 ± 0.25	
			19.0	175.14 ± 0.25	
2017 Sep 15	58,011.559 ± 0.003	H168	5.5	166.30 ± 1.10	−0.02 ± 0.01
			9.0	181.66 ± 0.36	
			17.0	178.47 ± 0.25	
			19.0	175.41 ± 0.30	
2017 Sep 16	58,012.55 ± 0.01	H168	5.5	164.00 ± 1.50	0.08 ± 0.01
			9.0	178.40 ± 1.90	
			17.0	184.15 ± 0.23	
			19.0	184.05 ± 0.34	
2017 Sep 17	58,013.553 ± 0.005	H168	5.5	135.40 ± 1.10	−0.18 ± 0.01
			9.0	141.77 ± 0.58	
			17.0	122.47 ± 0.24	
			19.0	118.64 ± 0.20	
2017 Sep 21	58,017.46 ± 0.09	H168	5.5	150.47 ± 0.08	−0.45 ± 0.01
			9.0	121.30 ± 2.00	
			17.0	91.81 ± 0.08	
			19.0	85.83 ± 0.07	
2017 Sep 23	58,019.52 ± 0.01	H168	5.5	377.20 ± 1.20	−0.46 ± 0.01

Table 3
(Continued)

Start Date (UT)	MJD	Telescope ^a Configuration	Central Frequency (GHz)	Flux Density (mJy)	α
2017 Sep 27	58,019.52 ± 0.02	H168	9.0	324.18 ± 0.34	−0.27 ± 0.01
			17.0	240.22 ± 0.35	
			19.0	223.18 ± 0.47	
2017 Sep 30	58,023.42 ± 0.02	H168	5.5	127.50 ± 0.29	−0.20 ± 0.01
			9.0	114.28 ± 0.15	
			17.0	95.24 ± 0.22	
2017 Oct 05	58,023.41 ± 0.03	H168	19.0	90.59 ± 0.25	−0.12 ± 0.02
			5.5	29.39 ± 0.23	
			9.0	26.84 ± 0.08	
2017 Oct 25	58,026.29 ± 0.01	H168	17.0	23.00 ± 0.05	0.08 ± 0.01
			19.0	23.52 ± 0.06	
			5.5	14.73 ± 0.22	
2017 Nov 02	58,031.40 ± 0.01	H168	9.0	13.32 ± 0.08	−0.71 ± 0.05
			17.0	12.87 ± 0.21	
			19.0	12.28 ± 0.23	
2017 Nov 23	58,031.40 ± 0.02	H168	5.5	75.91 ± 0.35	−0.70 ± 0.11
			9.0	82.61 ± 0.12	
			17.0	85.29 ± 0.19	
2017 Dec 03	58,051.33 ± 0.07	6A	19.0	87.20 ± 0.13	−0.30 ± 0.01
			5.5	42.57 ± 0.04	
			9.0	39.00 ± 0.16	
2017 Dec 10	58,051.388 ± 0.004	6A	17.0	30.01 ± 0.12	−0.64 ± 0.07
			19.0	29.12 ± 0.11	
			5.5	10.54 ± 0.12	
2017 Dec 16	58,059.84 ± 0.03	1.5C	9.0	7.44 ± 0.17	−1.0 ± 0.2
			17.0	0.35 ± 0.07	
			19.0	0.36 ± 0.09	
2017 Dec 23	58,080.24 ± 0.01	6C	5.5	0.63 ± 0.03	−0.75 ± 0.04
			9.0	0.74 ± 0.03	
			17.0	0.35 ± 0.07	
2017 Dec 30	58,090.78 ± 0.05	6C	19.0	0.36 ± 0.09	−0.60 ± 0.09
			5.5	0.63 ± 0.03	
			9.0	0.51 ± 0.02	
2018 Jan 05	58,090.79 ± 0.04	6C	17.0	0.28 ± 0.02	−0.89 ± 0.37
			19.0	0.44 ± 0.03	
			5.5	4.31 ± 0.22	
2018 Jan 12	58,097.80 ± 0.07	6C	9.0	3.53 ± 0.21	−0.26 ± 0.14
			17.0	2.24 ± 0.15	
			19.0	1.53 ± 0.20	
2018 Jan 21	58,103.92 ± 0.07	6C	5.5	2.20 ± 0.04	−0.55 ± 0.40
			9.0	1.39 ± 0.07	
			17.0	0.56 ± 0.08	
2018 Jan 27	58,103.93 ± 0.07	6C	19.0	0.48 ± 0.09	−0.42 ± 0.13
			5.5	1.21 ± 0.02	
			9.0	0.91 ± 0.03	
2018 Feb 02	58,110.98 ± 0.06	6C	17.0	0.54 ± 0.03	−0.26 ± 0.14
			19.0	0.39 ± 0.03	
			5.5	0.50 ± 0.02	
2018 Jan 05	58,110.98 ± 0.05	6C	9.0	0.45 ± 0.03	−0.60 ± 0.09
			17.0	0.21 ± 0.03	
			19.0	0.21 ± 0.04	
2018 Jan 12	58,117.93 ± 0.09	6C	5.5	0.18 ± 0.02	−0.89 ± 0.37
			9.0	0.11 ± 0.02	
			17.0	<0.12	
2018 Jan 21	58,117.98 ± 0.05	6C	19.0	<0.17	−0.26 ± 0.14
			5.5	0.32 ± 0.04	
			9.0	0.29 ± 0.03	
2018 Jan 27	58,123.80 ± 0.18	6C	17.0	0.25 ± 0.04	−0.55 ± 0.40
			19.0	0.22 ± 0.04	
			5.5	0.26 ± 0.04	
2018 Jan 27	58,123.82 ± 0.18	6C	9.0	0.20 ± 0.03	−0.55 ± 0.40
			17.0	<0.15	
			19.0	<0.22	
2018 Jan 27	58,123.82 ± 0.18	6C	5.5	0.31 ± 0.02	−0.42 ± 0.13
			9.0	0.11 ± 0.02	
			17.0	<0.12	
2018 Jan 27	58,130.93 ± 0.11	6C	19.0	<0.17	−0.26 ± 0.14
			5.5	0.32 ± 0.04	
			9.0	0.29 ± 0.03	
2018 Jan 27	58,130.94 ± 0.11	6C	17.0	0.25 ± 0.04	−0.55 ± 0.40
			19.0	0.22 ± 0.04	
			5.5	0.26 ± 0.04	
2018 Jan 27	58,130.94 ± 0.11	6C	9.0	0.20 ± 0.03	−0.55 ± 0.40
			17.0	<0.15	
			19.0	<0.22	
2018 Jan 27	58,139.73 ± 0.14	750A	5.5	0.31 ± 0.02	−0.42 ± 0.13
			9.0	0.28 ± 0.03	
			17.0	<0.15	
2018 Jan 27	58,139.73 ± 0.13	750A	5.5	0.31 ± 0.02	−0.42 ± 0.13
			9.0	0.28 ± 0.03	
			17.0	<0.15	
2018 Jan 27	58,146.09 ± 0.11	750A	5.5	0.31 ± 0.02	−0.42 ± 0.13
			9.0	0.28 ± 0.03	
			17.0	<0.15	
2018 Jan 27	58,146.09 ± 0.09	750A	5.5	0.31 ± 0.02	−0.42 ± 0.13
			9.0	0.28 ± 0.03	
			17.0	<0.15	
2018 Jan 27	58,146.09 ± 0.09	750A	5.5	0.31 ± 0.02	−0.42 ± 0.13
			9.0	0.28 ± 0.03	
			17.0	<0.15	
2018 Jan 27	58,146.09 ± 0.09	750A	5.5	0.31 ± 0.02	−0.42 ± 0.13
			9.0	0.28 ± 0.03	
			17.0	<0.15	

Table 3
(Continued)

Start Date (UT)	MJD	Telescope ^a Configuration	Central Frequency (GHz)	Flux Density (mJy)	α
	58,151.99 ± 0.07		17.0	0.19 ± 0.03	
2018 Feb 12	58,161.80 ± 0.07	750A	19.0	0.18 ± 0.04	-1.2 ± 0.6
			5.5	0.27 ± 0.06	
	58,161.80 ± 0.05		9.0	0.15 ± 0.03	
			17.0	<0.16	
2018 Feb 17	58,166.92 ± 0.13	750B	19.0	<0.22	
			5.5	<0.12	
			9.0	<0.06	
	58,166.94 ± 0.13		17.0	<0.11	
2018 Feb 22	58,172.00 ± 0.11	750B	19.0	<0.12	
			5.5	<0.1	
			9.0	<0.08	
	58,171.99 ± 0.09		17.0	<0.15	
2018 Feb 27	58,176.67 ± 0.18	750B	19.0	<0.18	
			5.5	<0.11	
			9.0	<0.09	
2018 Mar 11	58,188.48 ± 0.04	EW352	5.5	<0.14	
			9.0	<0.12	
2018 Mar 17	58,194.47 ± 0.05	EW352	5.5	<0.14	
			9.0	<0.11	
2018 Apr 13	58,221.77 ± 0.04	H168	5.5	<0.12	
			9.0	<0.11	
2018 Apr 14	58,222.83 ± 0.05	MeerKAT	1.3	<0.06	
2018 Apr 20	58,228.79 ± 0.07	H168	5.5	<0.08	
			9.0	<0.12	
2018 Apr 27	58,235.92 ± 0.03	H168	5.5	<0.19	
			9.0	<0.18	
	58,235.93 ± 0.03		17.0	<0.26	
			19.0	<0.28	
2018 May 03	58,241.93 ± 0.03	H168	5.5	<0.12	
			9.0	<0.13	
2018 May 06	58,244.92 ± 0.01	H168	5.5	<0.16	
			9.0	<0.17	
2018 May 11	58,249.91 ± 0.01	6D	5.5	<0.16	
			9.0	<0.16	

Notes. Observation MJDs represent the middle of the observation, where errors represent the observation duration. 1σ flux density errors are uncertainties to the fitted source model. Upper limits are three times the image rms at the source position.

^a https://www.narrabri.atnf.csiro.au/operations/array_configurations/configurations.html

Table 4
Radio Flux Densities of S2

Start Date (UT)	MJD	Telescope ⁹ Configuration	Central Frequency (GHz)	Flux Density (mJy)	α
2017 Dec 03	58,090.78 ± 0.05	6C	5.5	2.87 ± 0.07	-0.71 ± 0.02
			9.0	1.98 ± 0.03	
	58,090.79 ± 0.04		17.0	1.28 ± 0.06	
			19.0	1.23 ± 0.07	
2017 Dec 10	58,097.80 ± 0.07	6C	5.5	0.98 ± 0.05	-0.82 ± 0.03
			9.0	0.65 ± 0.04	
	58,097.82 ± 0.06		17.0	0.37 ± 0.02	
			19.0	0.40 ± 0.04	
2017 Dec 16	58,103.92 ± 0.07	6C	5.5	0.39 ± 0.06	-0.8 ± 0.3
			9.0	0.26 ± 0.06	
2017 Dec 23	58,110.98 ± 0.06	6C	5.5	0.45 ± 0.05	-0.5 ± 0.1
			9.0	0.40 ± 0.08	
	58,110.98 ± 0.05		17.0	0.27 ± 0.09	
			19.0	0.22 ± 0.09	
2017 Dec 30	58,117.93 ± 0.09	6C	5.5	0.19 ± 0.02	-0.48 ± 0.08

Table 4
(Continued)

Start Date (UT)	MJD	Telescope ⁹ Configuration	Central Frequency (GHz)	Flux Density (mJy)	α
			9.0	0.16 ± 0.02	
	58,117.98 ± 0.05		17.0	0.11 ± 0.03	
			19.0	0.09 ± 0.03	
2018 Jan 05	58,123.80 ± 0.18	6C	5.5	0.17 ± 0.02	-0.55 ± 0.22
			9.0	0.13 ± 0.03	
	58,123.82 ± 0.18		17.0	<0.09	
			19.0	<0.12	
2018 Jan 12	58,130.93 ± 0.11	6C	5.5	0.14 ± 0.02	-0.8 ± 0.2
			9.0	0.10 ± 0.02	
	58,130.94 ± 0.11		17.0	<0.12	
			19.0	<0.18	
2018 Jan 21	58,139.73 ± 0.14	750A	5.5	0.17 ± 0.04	-1.0 ± 0.35
			9.0	0.10 ± 0.03	
	58,139.73 ± 0.13		17.0	<0.12	
			19.0	<0.12	
2018 Jan 27	58,146.09 ± 0.11	750A	5.5	<0.12	
			9.0	<0.09	
2018 Feb 02	58,151.99 ± 0.09	750A	5.5	<0.06	
			9.0	<0.09	
2018 Mar 17	58,194.47 ± 0.05	EW352	5.5	<0.14	
			9.0	<0.11	
2018 Apr 13	58,221.77 ± 0.04	H168	5.5	<0.12	
			9.0	<0.11	
2018 Apr 14	58,222.83 ± 0.05	MeerKAT	1.3	0.29 ± 0.05	
2018 Apr 20	58,228.79 ± 0.07	H168	5.5	<0.08	
			9.0	<0.12	
2018 Apr 27	58,235.92 ± 0.03	H168	5.5	<0.19	
			9.0	<0.18	
	58,235.93 ± 0.03		17.0	<0.26	
			19.0	<0.28	
2018 May 03	58,241.93 ± 0.03	H168	5.5	<0.12	
			9.0	<0.13	
2018 May 03	58,241.93 ± 0.03	H168	5.5	<0.12	
			9.0	<0.13	
2018 May 06	58,244.92 ± 0.01		5.5	<0.16	
			9.0	<0.17	
2018 May 11	58,249.91 ± 0.01	6D	5.5	<0.16	
			9.0	<0.16	
2018 May 14	58,252.79 ± 0.12	6D	5.5	0.13 ± 0.01	-0.35 ± 0.25
			9.0	0.11 ± 0.02	
2018 May 17	58,255.37 ± 0.08	6D	5.5	0.20 ± 0.02	-0.37 ± 0.25
			9.0	0.17 ± 0.04	
2018 May 20	58,258.45 ± 0.10	6D	5.5	<0.15	
			9.0	<0.15	
2018 May 31	58,269.28 ± 0.03	6D	5.5	<0.12	
			9.0	<0.09	
2018 Jun 01	58,270.30 ± 0.01	6D	5.5	<0.12	
			9.0	<0.095	
2018 Aug 05	58,335.66 ± 0.03	H75	5.5	<0.48	
			9.0	<0.35	
2018 Oct 02	58,393.36 ± 0.09	750C	5.5	0.15 ± 0.02	-1.0 ± 0.3
			9.0	0.09 ± 0.02	
2018 Oct 14	58,405.09 ± 0.03	6A	5.5	<0.15	
			9.0	<0.09	

Notes. Observation MJDs represent the middle of the observation, where errors represent the observation duration. We also include non-detection close in time to the detections to emphasize the brightenings at late times. 1σ errors are uncertainties to the fitted source model. Upper limits are three times the image rms at the target position.

⁹ https://www.narrabri.atnf.csiro.au/operations/array_configurations/configurations.html

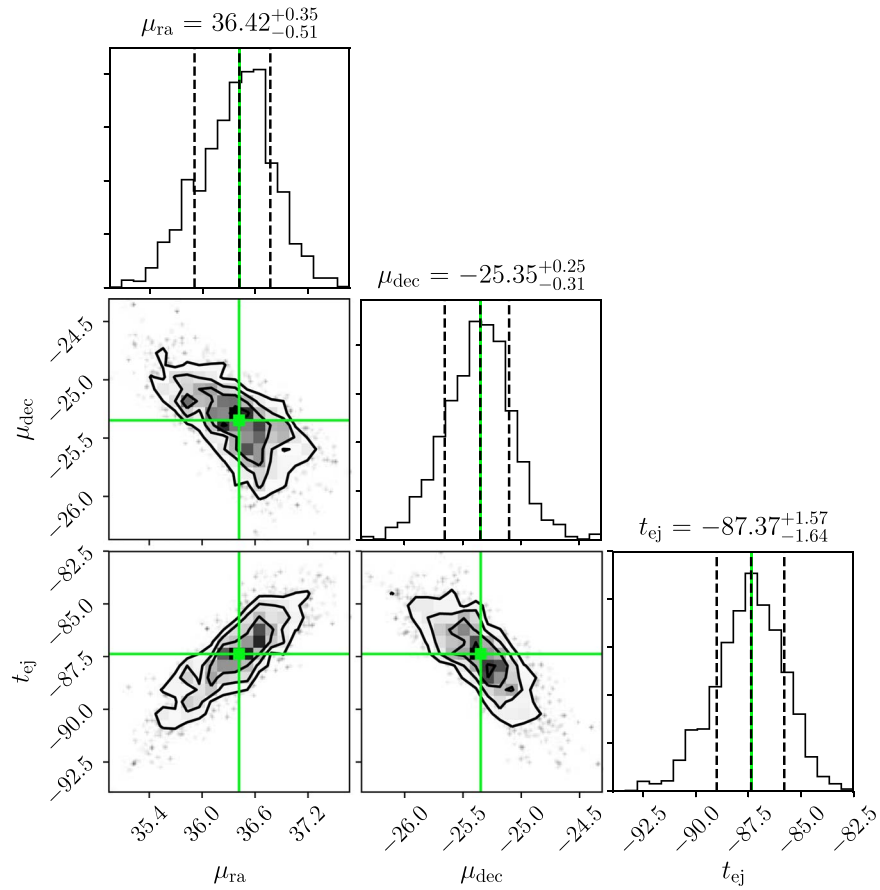


Figure 10. Correlation plots of parameters for the simple bulk motion model. Here we show the proper motion in R.A. ($\mu_{R.A.}$) and decl. ($\mu_{decl.}$), as well as the best-fit date of the ejection (t_{ej}), normalized to the MJD of the first S2 detection (MJD 58,090.78). The histograms represent the one-dimensional posterior distributions of the parameters, and the green lines/squares indicate the best-fit value of the parameters.

Table 5

Measured (Corrected) Positions of S2 and the Separation from R.A. = $15^h35^m19^s.71'$, decl. = $-57^d13^m47^s.58$ (Errors Are Statistical Errors on the Fitted Position)

Start Date (UT)	MJD	R.A.	Decl.	Separation	
				R.A. (")	Decl. (")
2017 Dec 03	$58,090.78 \pm 0.05$	$15^h35^m20.12^s \pm 0''.18$	$-57^\circ13' 49''.92 \pm 0''.09$	3.33 ± 0.18	-2.34 ± 0.09
2017 Dec 10	$58,097.80 \pm 0.07$	$15^h35^m20.15^s \pm 0''.13$	$-57^\circ13' 50''.03 \pm 0''.06$	3.61 ± 0.13	-2.45 ± 0.06
2017 Dec 16	$58,103.92 \pm 0.07$	$15^h35^m20.11^s \pm 0''.10$	$-57^\circ13' 49''.64 \pm 0''.14$	3.28 ± 0.10	-2.06 ± 0.14
2017 Dec 23	$58,110.98 \pm 0.06$	$15^h35^m20.18^s \pm 0''.07$	$-57^\circ13' 49''.96 \pm 0''.20$	3.84 ± 0.07	-2.38 ± 0.20
2018 Dec 30	$58,117.93 \pm 0.09$	$15^h35^m20.21^s \pm 0''.13$	$-57^\circ13' 50''.25 \pm 0''.29$	4.08 ± 0.13	-2.67 ± 0.29
2018 Jan 05	$58,123.80 \pm 0.18$	$15^h35^m20.24^s \pm 0''.12$	$-57^\circ13' 50''.67 \pm 0''.11$	4.33 ± 0.12	-3.09 ± 0.11
2018 Jan 12	$58,130.93 \pm 0.11$	$15^h35^m20.30^s \pm 0''.13$	$-57^\circ13' 50''.88 \pm 0''.26$	4.78 ± 0.13	-3.30 ± 0.26
2018 Jan 21	$58,139.73 \pm 0.14$	$15^h35^m20.35^s \pm 0''.23$	$-57^\circ13' 51''.45 \pm 0''.23$	5.19 ± 0.23	-3.87 ± 0.23
2018 Apr 14	$58,222.83 \pm 0.05$	$15^h35^m20.71^s \pm 0''.95$	$-57^\circ13' 52''.41 \pm 0''.40$	8.12 ± 0.95	-4.83 ± 0.40
2018 May 14	$58,252.79 \pm 0.12$	$15^h35^m20.88^s \pm 0''.12$	$-57^\circ13' 54''.16 \pm 0''.08$	9.52 ± 0.12	-6.58 ± 0.08
2018 May 17	$58,255.37 \pm 0.12$	$15^h35^m20.86^s \pm 0''.20$	$-57^\circ13' 54''.00 \pm 0''.11$	9.33 ± 0.20	-6.42 ± 0.11
2018 Oct 02	$58,393.36 \pm 0.09$	$15^h35^m21.40^s \pm 0''.18$	$-57^\circ13' 56''.78 \pm 0''.16$	13.72 ± 0.18	-9.20 ± 0.16

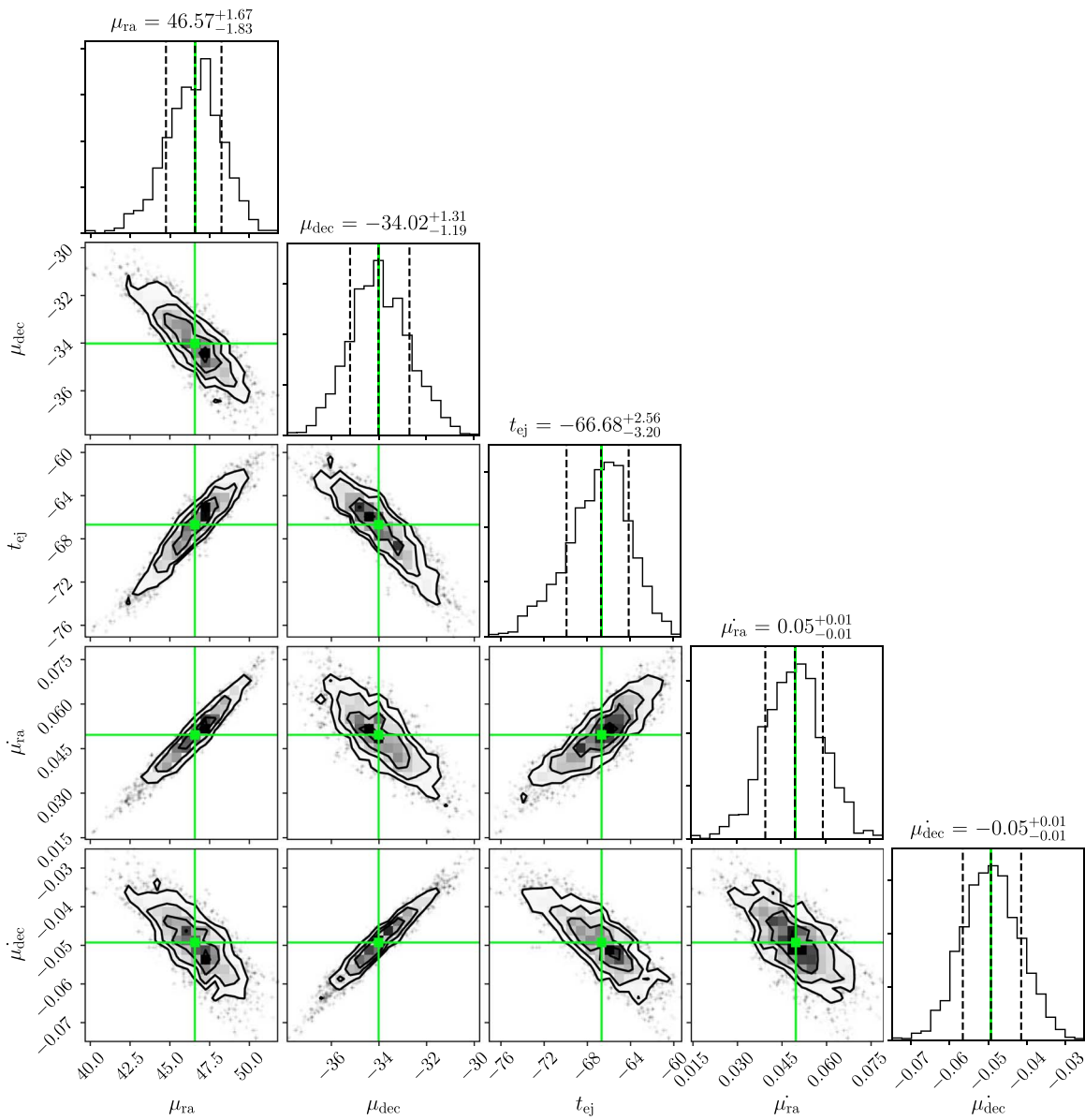


Figure 11. Correlation plots of parameters for the deceleration model. Here we show the average proper motion in R.A. ($\mu_{\text{R.A.}}$) and decl. ($\mu_{\text{decl.}}$), the best-fit date of the ejection (t_{ej}) normalized to the MJD of the first S2 detection, MJD 58,090.78, and the average acceleration in both R.A. and decl. ($\dot{\mu}_{\text{R.A.}}$ and $\dot{\mu}_{\text{decl.}}$, respectively). The histograms represent the one-dimensional posterior distributions of the parameters, and the green lines/squares indicate the best-fit value of the parameters.

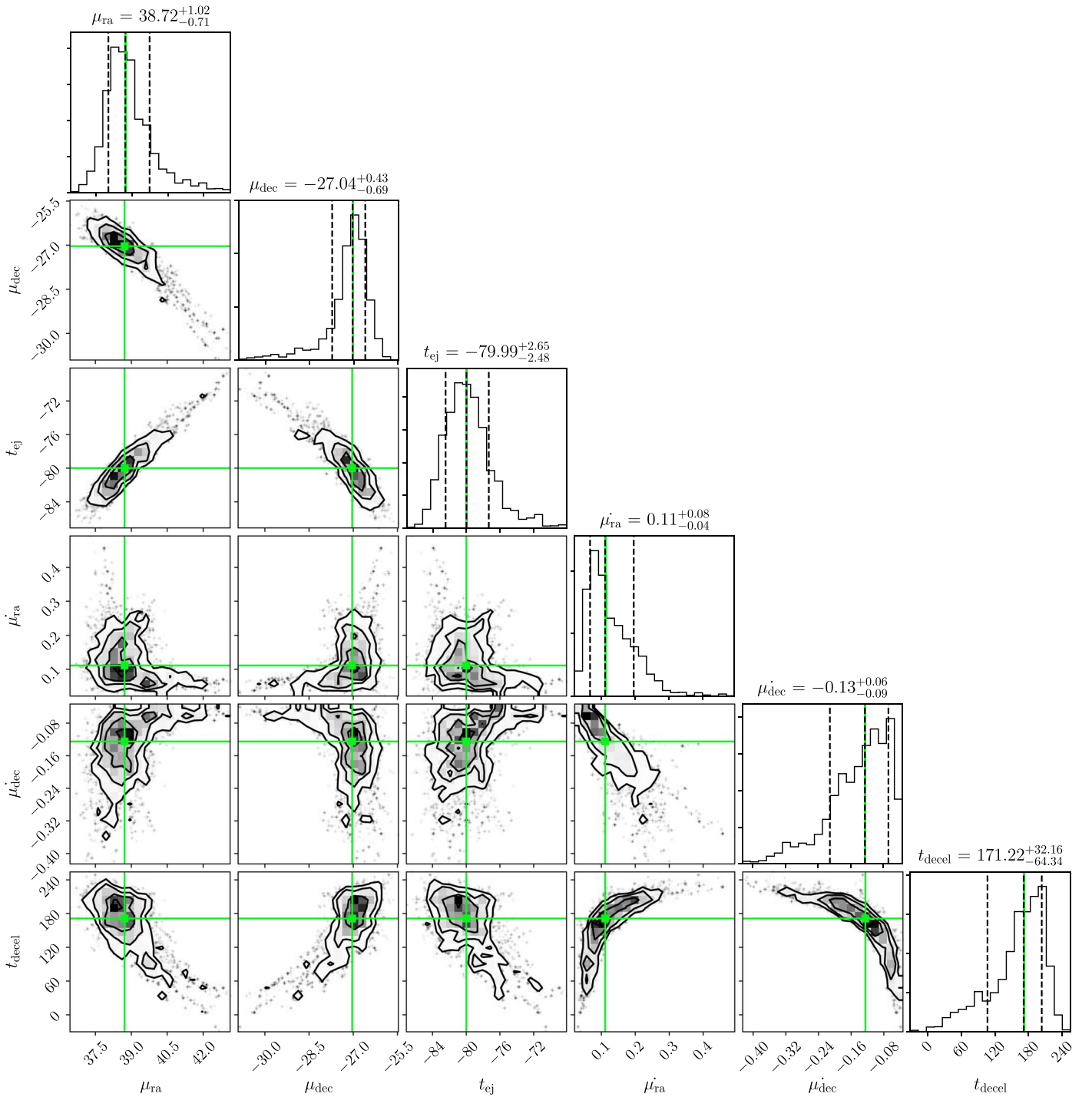


Figure 12. Correlation plots of parameters for the combined bulk plus deceleration model. Here we show the average proper motion in R.A. ($\mu_{R.A.}$) and decl. ($\mu_{decl.}$), the best-fit date of the ejection (t_{ej}) normalized to the MJD of the first S2 detection, MJD 58,090.78, the average acceleration in both R.A. and decl. ($\dot{\mu}_{R.A.}$ and $\dot{\mu}_{decl.}$, respectively), and the deceleration start date t_{decel} . The histograms represent the one-dimensional posterior distributions of the parameters, and the green lines/squares indicate the best-fit value of the parameters.

ORCID iDs

T. D. Russell <https://orcid.org/0000-0002-7930-2276>
 A. J. Tetarenko <https://orcid.org/0000-0003-3906-4354>
 J. C. A. Miller-Jones <https://orcid.org/0000-0003-3124-2814>
 G. R. Sivakoff <https://orcid.org/0000-0001-6682-916X>
 E. Tremou <https://orcid.org/0000-0002-4039-6703>
 M. C. Baglio <https://orcid.org/0000-0003-1285-4057>

S. Markoff <https://orcid.org/0000-0001-9564-0876>
 R. Soria <https://orcid.org/0000-0002-4622-796X>

References

Arnaud, K. A. 1996, in ASP Conf. Ser. 101, *Astronomical Data Analysis Software and Systems V*, ed. G. H. Jacoby & J. Barnes (San Francisco, CA: ASP), 17
 Astropy Collaboration, Robitaille, T. P., Tollerud, E. J., et al. 2013, *A&A*, 558, A33
 Baglio, M. C., Russell, D. M., Casella, P., et al. 2018, *ApJ*, 867, 114

- Bahramian, A., Miller-Jones, J. C. A., Strader, J., et al. 2018, Radio/X-ray Correlation Database for X-ray Binaries, Zenodo, doi:10.5281/zenodo.1252036
- Barkana, R., & Loeb, A. 2001, *PhR*, **349**, 125
- Begelman, M. C., & Armitage, P. J. 2014, *ApJL*, **782**, L18
- Belloni, T., Homan, J., Casella, P., et al. 2005, *A&A*, **440**, 207
- Belloni, T. M. 2010, *The Jet Paradigm: From Microquasars to Quasars* (Berlin: Springer), 53
- Bhargava, Y., Belloni, T., Bhattacharya, D., & Misra, R. 2019, *MNRAS*, **488**, 720
- Brocksopp, C., Miller-Jones, J. C. A., Fender, R. P., & Stappers, B. W. 2007, *MNRAS*, **378**, 1111
- Camilo, F., Scholz, P., Serylak, M., et al. 2018, *ApJ*, **856**, 180
- Casella, P., Belloni, T., & Stella, L. 2005, *ApJ*, **629**, 403
- Ceccobello, C., Cavecchi, Y., Heemskerck, M. H. M., et al. 2018, *MNRAS*, **473**, 4417
- Chauhan, J., Miller-Jones, J. C. A., Anderson, G. E., et al. 2019, *MNRAS*, **488**, 129
- Corbel, S., Aussel, H., Broderick, J. W., et al. 2013b, *MNRAS*, **431**, L107
- Corbel, S., Coriat, M., Brocksopp, C., et al. 2013a, *MNRAS*, **428**, 2500
- Corbel, S., & Fender, R. P. 2002, *ApJL*, **573**, L35
- Corbel, S., Fender, R. P., Tomsick, J. A., Tzioumis, A. K., & Tingay, S. 2004, *ApJ*, **617**, 1272
- Corbel, S., Fender, R. P., Tzioumis, A. K., et al. 2000, *A&A*, **359**, 251
- Corbel, S., Fender, R. P., Tzioumis, A. K., et al. 2002, *Sci*, **298**, 196
- Corbel, S., Kaaret, P., Fender, R. P., et al. 2005, *ApJ*, **632**, 504
- Corbel, S., Nowak, M. A., Fender, R. P., Tzioumis, A. K., & Markoff, S. 2003, *A&A*, **400**, 1007
- Coriat, M., Corbel, S., Prat, L., et al. 2011, *MNRAS*, **414**, 677
- Curran, P. A., Coriat, M., Miller-Jones, J. C. A., et al. 2014, *MNRAS*, **437**, 3265
- Dhawan, V., Mirabel, I. F., & Rodríguez, L. F. 2000, *ApJ*, **543**, 373
- Dincer, T. 2017, ATel, 10716
- Drappeau, S., Malzac, J., Coriat, M., et al. 2017, *MNRAS*, **466**, 4272
- Dunn, R. J. H., Fender, R. P., Körding, E. G., Belloni, T., & Cabanac, C. 2010, *MNRAS*, **403**, 61
- Espinasse, M., & Fender, R. 2018, *MNRAS*, **473**, 4122
- Fabian, A. C. 2012, *ARA&A*, **50**, 455
- Fender, R. 2006, in *Jets from X-ray Binaries*, ed. W. H. G. Lewin & M. van der Klis (Cambridge: Cambridge Univ. Press), 381
- Fender, R., & Gallo, E. 2014, *SSRv*, **183**, 323
- Fender, R. P. 2001, *MNRAS*, **322**, 31
- Fender, R. P., Belloni, T. M., & Gallo, E. 2004, *MNRAS*, **355**, 1105
- Fender, R. P., Garrington, S. T., McKay, D. J., et al. 1999, *MNRAS*, **304**, 865
- Fender, R. P., Homan, J., & Belloni, T. M. 2009, *MNRAS*, **396**, 1370
- Fender, R. P., Rayner, D., McCormick, D. G., et al. 2002, *MNRAS*, **336**, 39
- Fender, R., Woudt, P. A., Armstrong, R., et al. 2017, arXiv:1711.04132
- Fendt, C., & Sheikhnezami, S. 2013, *ApJ*, **774**, 12
- Foreman-Mackey, D., Hogg, D. W., Lang, D., & Goodman, J. 2013, *PASP*, **125**, 306
- Gallo, E., et al. 2014, *MNRAS*, **445**, 290
- Gallo, E., Corbel, S., Fender, R. P., Maccarone, T. J., & Tzioumis, A. K. 2004, *MNRAS*, **347**, L52
- Gallo, E., Degenaar, N., & van den Eijnden, J. 2018, *MNRAS*, **478**, L132
- Gallo, E., Fender, R., Kaiser, C., et al. 2005, *Natur*, **436**, 819
- Gallo, E., Fender, R. P., & Pooley, G. G. 2003, *MNRAS*, **344**, 60
- Gallo, E., Miller, B. P., & Fender, R. 2012, *MNRAS*, **423**, 590
- Hjellming, R. M., & Rupen, M. P. 1995, *Natur*, **375**, 464
- Homan, J., Wijnands, R., van der Klis, M., et al. 2001, *ApJS*, **132**, 377
- Huang, Y., Qu, J. L., Zhang, S. N., et al. 2018, *ApJ*, **866**, 122
- Ingram, A., Done, C., & Fragile, P. C. 2009, *MNRAS*, **397**, L101
- Jamil, O., Fender, R. P., & Kaiser, C. R. 2010, *MNRAS*, **401**, 394
- Jonas, J. & MeerKAT Team 2016, MeerKAT Science: On the Pathway to the SKA in The MeerKAT Telescope (Trieste: SISSA), 001
- Kaaret, P., Corbel, S., Tomsick, J. A., et al. 2003, *ApJ*, **582**, 945
- Kalemci, E., Dinçer, T., Tomsick, J. A., et al. 2013, *ApJ*, **779**, 95
- Kennea, J. A., Evans, P. A., Beardmore, A. P., et al. 2017, ATel, 10700
- King, A. L., Miller, J. M., Bietenholz, M., et al. 2016, *NatPh*, **12**, 772
- Klein-Wolt, M., & van der Klis, M. 2008, *ApJ*, **675**, 1407
- Koljonen, K. I. I., Hannikainen, D. C., McCollough, M. L., Pooley, G. G., & Trushkin, S. A. 2010, *MNRAS*, **406**, 307
- Koljonen, K. I. I., Maccarone, T., McCollough, M. L., et al. 2018, *A&A*, **612**, A27
- Krimm, H. A., Holland, S. T., Corbet, R. H. D., et al. 2013, *ApJS*, **209**, 14
- Kylafis, N. D., & Belloni, T. M. 2015, *A&A*, **574**, A133
- Kylafis, N. D., Contopoulos, I., Kazanas, D., & Christodoulou, D. M. 2012, *A&A*, **538**, A5
- Lepingwell, V. A., Bazzano, A., Bird, A. J., et al. 2018, ATel, 11884
- Lisakov, M. M., Kovalev, Y. Y., Savolainen, T., Hovatta, T., & Kutkin, A. M. 2017, *MNRAS*, **468**, 4478
- Liska, M., Hesp, C., Tchekhovskoy, A., et al. 2018, *MNRAS*, **474**, L81
- Maccarone, T. J. 2003, *A&A*, **409**, 697
- Malzac, J. 2013, *MNRAS*, **429**, L20
- Markoff, S., Falcke, H., & Fender, R. 2001, *A&A*, **372**, L25
- Markoff, S., Nowak, M. A., & Wilms, J. 2005, *ApJ*, **635**, 1203
- Markwardt, C. B., Burrows, D. N., Cummings, J. R., et al. 2017, GCN, 21788
- Marscher, A. P., Jorstad, S. G., D'Arcangelo, F. D., et al. 2008, *Natur*, **452**, 966
- Martí-Vidal, I., Vlemmings, W. H. T., Muller, S., & Casey, S. 2014, *A&A*, **563**, A136
- McMullin, J. P., Waters, B., Schiebel, D., Young, W., & Golap, K. 2007, in ASP Conf. Ser. 376, *Astronomical Data Analysis Software and Systems XVI*, ed. R. A. Shaw, F. Hill, & D. J. Bell (San Francisco, CA: ASP), 127
- Migliori, G., Corbel, S., Tomsick, J. A., et al. 2017, *MNRAS*, **472**, 141
- Miller, J. M., Gendreau, K., Ludlam, R. M., et al. 2018, *ApJL*, **860**, L28
- Miller-Jones, J. C. A., Fender, R. P., & Nakar, E. 2006, *MNRAS*, **367**, 1432
- Miller-Jones, J. C. A., Jonker, P. G., Ratti, E. M., et al. 2011, *MNRAS*, **415**, 306
- Miller-Jones, J. C. A., Moin, A., Tingay, S. J., et al. 2012a, *MNRAS*, **419**, L49
- Miller-Jones, J. C. A., Sivakoff, G. R., Altamirano, D., et al. 2012b, *MNRAS*, **421**, 468
- Miller-Jones, J. C. A., Tetarenko, A. J., Sivakoff, G. R., et al. 2019, *Natur*, **569**, 374
- Mioduszewski, A. J., Rupen, M. P., Hjellming, R. M., Pooley, G. G., & Waltman, E. B. 2001, *ApJ*, **553**, 766
- Mirabel, I. F., Dijkstra, M., Laurent, P., Loeb, A., & Pritchard, J. R. 2011, *A&A*, **528**, A149
- Mirabel, I. F., & Rodríguez, L. F. 1994, *Natur*, **371**, 46
- Mirabel, I. F., & Rodríguez, L. F. 1999, *ARA&A*, **37**, 409
- Nakahira, S., Shidatsu, M., Makishima, K., et al. 2018, *PASJ*, **70**, 95
- Narayan, R., & Yi, I. 1995, *ApJ*, **452**, 710
- Negoro, H., Miyoshi, S., Ozawa, H., et al. 2010, ASP Conf. Ser. 434 in *Astronomical Data Analysis Software and Systems XIX*, ed. Y. Mizumoto, K.-I. Morita, & M. Ohishi (San Francisco, CA: ASP), 127
- Negoro, H., Ishikawa, M., Ueno, S., et al. 2017a, ATel, 10699
- Negoro, H., Kawase, T., Sugizaki, M., et al. 2017b, ATel, 10708
- Negoro, H., Sugawara, Y., Nakajima, M., et al. 2018, ATel, 11682
- Offringa, A. R. 2010, AOFlogger: RFI Software, Astrophysics Source Code Library, ascl:1010.017
- Parikh, A. S., Russell, T. D., Wijnands, R., et al. 2018, ATel, 11652
- Parikh, A. S., Russell, T. D., Wijnands, R., et al. 2019, *ApJL*, **878**, L28
- Petrucci, P.-O., Ferreira, J., Henri, G., & Pelletier, G. 2008, *MNRAS*, **385**, L88
- Rapisarda, S., Ingram, A., & van der Klis, M. 2014, *MNRAS*, **440**, 2882
- Rees, M. J. 1966, *Natur*, **211**, 468
- Remillard, R. A., Muno, M. P., McClintock, J. E., & Orosz, J. A. 2002, *ApJ*, **580**, 1030
- Rodríguez, L. F., & Mirabel, I. F. 1999, *ApJ*, **511**, 398
- Romero, G. E., Boettcher, M., Markoff, S., & Tavecchio, F. 2017, *SSRv*, **207**, 5
- Rupen, M. P., Hjellming, R. M., & Mioduszewski, A. J. 1998, IAUC, 6938
- Rushton, A. P., Miller-Jones, J. C. A., Curran, P. A., et al. 2017, *MNRAS*, **468**, 2788
- Russell, D. M., Fender, R. P., Gallo, E., & Kaiser, C. R. 2007, *MNRAS*, **376**, 1341
- Russell, D. M., Miller-Jones, J. C. A., Maccarone, T. J., et al. 2011, *ApJL*, **739**, L19
- Russell, D. M., Markoff, S., Casella, P., et al. 2013a, *MNRAS*, **429**, 815
- Russell, D. M., Russell, T. D., Miller-Jones, J. C. A., et al. 2013b, *ApJL*, **768**, L35
- Russell, T. D., Miller-Jones, J. C. A., Sivakoff, G. R., Tetarenko, A. J. & Jacpot Xrb Collaboration 2017, ATel, 10711
- Russell, T. D., Soria, R., Miller-Jones, J. C. A., et al. 2014, *MNRAS*, **439**, 1390
- Scaringi, S. & ASTR211 Students 2017a, ATel, 10702
- Scaringi, S. & ASTR211 Students 2017b, ATel, 10704
- Shibata, K., & Uchida, Y. 1986, *PASJ*, **38**, 631
- Sikora, M., Begelman, M. C., Madejski, G. M., & Lasota, J.-P. 2005, *ApJ*, **625**, 72
- Silk, J., & Rees, M. J. 1998, *A&A*, **331**, L1
- Smirnov, O. M., & Tasse, C. 2015, *MNRAS*, **449**, 2668
- Sreehari, H., Ravishankar, B. T., Iyer, N., et al. 2019, *MNRAS*, **487**, 928
- Stevens, A. L., Uttley, P., Altamirano, D., et al. 2018, *ApJL*, **865**, L15

- Stirling, A. M., Spencer, R. E., de la Force, C. J., et al. 2001, [MNRAS](#), **327**, 1273
- Tao, L., Chen, Y., Güngör, C., et al. 2018, [MNRAS](#), **480**, 4443
- Tasse, C., Hugo, B., Mirmont, M., et al. 2018, [A&A](#), **611**, 87
- Tetarenko, A. J., Freeman, P., Rosolowsky, E. W., Miller-Jones, J. C. A., & Sivakoff, G. R. 2018, [MNRAS](#), **475**, 448
- Tetarenko, A. J., Russell, T. D., Miller-Jones, J. C. A., Sivakoff, G. R. & Japcot Xrb Collaboration 2017a, ATel, 10745
- Tetarenko, A. J., Sivakoff, G. R., Miller-Jones, J. C. A., et al. 2017b, [MNRAS](#), **469**, 3141
- Tingay, S. J., Jauncey, D. L., Preston, R. A., et al. 1995, [Natur](#), **374**, 141
- Tomsick, J. A., Yamaoka, K., Corbel, S., et al. 2014, [ApJ](#), **791**, 70
- Vahdat Motlagh, A., Kalemci, E., & Maccarone, T. J. 2019, [MNRAS](#), **485**, 2744
- van der Horst, A. J., Curran, P. A., Miller-Jones, J. C. A., et al. 2013, [MNRAS](#), **436**, 2625
- Verner, D. A., Ferland, G. J., Korista, K. T., & Yakovlev, D. G. 1996, [ApJ](#), **465**, 487
- Wijnands, R., Homan, J., & van der Klis, M. 1999, [ApJL](#), **526**, L33
- Wilms, J., Allen, A., & McCray, R. 2000, [ApJ](#), **542**, 914
- Xu, Y., Brocksopp, C., Corbel, S., et al. 2018, [ApJL](#), **852**, L34
- Yang, J., Brocksopp, C., Corbel, S., et al. 2010, [MNRAS](#), **409**, L64